DISSERTATION

YTTRIUM IRON GARNET NANO FILMS: EPITAXIAL GROWTH, DAMPING, SPIN PUMPING, AND MAGNETIC PROXIMITY EFFECT

Submitted by

Yiyan Sun

Department of Physics

In partial fulfillment of the requirements

For the Degree of Doctor of Philosophy

Colorado State University

Fort Collins, Colorado

Spring 2014

Doctoral Committee:

Advisor: Mingzhong Wu

Carl Patton
Stuart Field
Steven Reising
Zbigniew Celinski

ABSTRACT

YTTRIUM IRON GARNET NANO FILMS: EPITAXIAL GROWTH, DAMPING, SPIN PUMPING, AND MAGNETIC PROXIMITY EFFECT

Recently, a new research field called magnetic insulator-based spintronics opened the door to a large amount of potential applications in the electronics industry. In this field, low-damping materials in the nanometer scale are critically needed for both fundamental studies, such as spin pumping, and device applications, such as spin-torque nano-oscillators. Yttrium iron garnet (YIG) materials are the best candidate among other materials. There is a critical demand for high-quality nanometer-thick YIG films.

This dissertation reports experimental studies on YIG films with the thickness ranged from several nanometers to several hundreds of nanometers. Firstly, the feasibility of low-damping YIG nano films growth via pulsed laser deposition (PLD) techniques is demonstrated. A 5-nm-thick YIG film, for example, shows a peak-to-peak ferromagnetic resonance (FMR) linewidth of <10 Oe at 10 GHz. Optimization of PLD control parameters and post-deposition annealing processes and surface modification by ion beam etching for the realization of high-quality films are discussed in detail.

The second main topic is on spin pumping and magnetic proximity effects in YIG nano films. Specifically, the dissertation touches on (1) the spin pumping efficiency of YIG nano films and (2) damping enhancement in YIG nano films due to Pt capping layers. Knowing the efficiency of spin angular momentum transfers across YIG/normal metal (NM) interfaces is critical to the use of YIG films for spintronics. Under subtopic (1), the spin transfer efficiency

at YIG/NM interfaces is determined through the measurement of spin pumping-caused additional damping in YIG nano films. A fairly large portion of recent studies on YIG-based spintronics made use of a Pt capping layer either as a detector to measure spin currents or as a spin-current source. Work under subtopic (2), however, indicates that the growth of a Pt capping layer onto a YIG film can result in a significant damping enhancement in the YIG film. Fortunately, this damping can be completely suppressed simply by the addition of a thin Cu spacer in-between the YIG and Pt films. The interpretation of the observed damping enhancement in terms of the magnetic proximity effect in the Pt film is presented.

The last topic addresses the growth of high-quality YIG thin films on metallic substrates. It is demonstrated that one can grow YIG thin films on Cu via the use of a protection layer of high entropy alloy nitrides. The YIG films showed a peak-to-peak FMR linewidth of about 1.1 Oe at 9.45 GHz. This work provides implications for the future development of YIG thin film-based monolithic devices for high frequency processing.

ACKNOWLEDGEMENTS

First of all, I would like to send the deepest gratitude to my advisor, Professor Mingzhong Wu. This dissertation would have been a lot more difficult to finish without his advice. Professor Wu spent a lot of time on the detailed discussions of my research work and made countless efforts to help revise this dissertation. His professional attitude, hard-working character, self-motivation, and enthusiasm for high-level research has had deep influence on my studies.

My appreciation also extends to every member in the Magnetics Laboratory at CSU. Their knowledge, experience, and skills were very valuable assets to me. We established many good friendships during our daily collaborations. Especially, grateful thanks go to Dr. Young-Yeal Song. He taught me how to hand fabricate high-quality samples and provided me with a foundation of knowledge in magnetic materials. I also want to send my sincerest thanks to Professor Carl Patton, who taught me how to become a successful scientific researcher. He also provided me with valuable suggestions on my dissertation work. In addition, I want to express my gratitude to other researchers: Zihui Wang, who helped me a lot in the material and device testing, Lei Lu, who provided me with very useful information about the ferromagnetic resonance measurements, and Houchen Chang, who helped with the sample fabrications and characterizations, as well as Mike Kabatek, Praveen Janantha, David Ellsworth, and William Schneider, who helped edit this dissertation.

Last but not least, I would like to thank my wife, Shasha Liu. She always encouraged me to have an optimistic attitude towards research. Without her support, I wouldn’t be able to complete my Ph.D. program.

TABLE OF CONTENTS

CHAPTER 1

OVERVIEW

1.1 Background and motivations

The year of 2010 witnesses two significant discoveries in the field of spintronics: (1) transfer of electrical signals with magnetic insulators[1] and (2) spin Seebeck effects in magnetic insulators.[2,3] The magnetic insulators used in both discoveries were magnetic garnets, which Dr. Kittel referred to as the fruitfly of magnetism about 50 years ago.[4] For (1), an initial electrical signal excites a spin wave in one end of an yttrium iron garnet ($Y_3Fe_5O_{12}$, YIG) film strip via the spin Hall effect; as the spin wave travels to the other end of the YIG strip, it is converted to an electrical signal via the inverse spin Hall effect. For (2), one establishes a temperature gradient along a YIG or $LaY_3Fe_5O_{12}$ film strip, and the latter produces a difference between the chemical potentials of spin-up and spin-down electrons in the film strip. This potential difference, also called a spin voltage, can generate a spin current in a normal metal

[1] Y. Kajiwara, K. Harii, S. Takahashi, J. Ohe, K. Uchida, M. Mizuguchi, H. Umezawa, H. Kawai, K. Ando, K. Takanashi, S. Maekawa, and E. Saitoh, Nature **464**, 262 (2010).
[2] K. Uchida, J. Xiao, H. Adachi, J. Ohe, S. Takahashi, J. Leda, T. Ota, Y. Kajiwara, H. Umezawa, H. Kawai, G. E. W. Bauer, S. Maekawa, and E. Saitoh, Nature Materials **9**, 894 (2010).
[3] K. Uchida, H. Adachi, T. Ota, H. Nakayama, S. Maekawa, and E. Saitoh, Appl. Phys. Lett. **97**, 172505 (2010).
[4] P. E. Wigen, R. D. McMichael, and C. Jayaprakash, J. Magn. Magn. Mater. **84**, 237 (1990).

layer deposited on the end of the film strip. Although several features related to these effects remain unexplained, the effects clearly demonstrate that one can transmit spin currents into and out of magnetic garnets as well as use magnetic garnets to generate spin currents. This demonstration opens a new paradigm in the discipline of spintronics and opens the door to a new class of spintronic devices that make use of either pure YIG or doped YIG materials.[5,6]

It should be noted that, thanks to the absence of conduction electrons and Fe^{2+} ions, magnetic garnets generally have slower ferromagnetic relaxation than other ferrimagnetic materials.[7] Moreover, in the family of magnetic garnets, YIG and doped YIG have the lowest relaxation rates. Indeed, YIG materials have a relaxation rate lower than any other magnetic materials, with an intrinsic damping constant α of about 3×10^{-5} only. Because of this extremely small damping, YIG materials have found rather broad current and potential applications in microwave devices.[8,9,10] YIG sphere-based oscillators and filters, for example, are core devices in many microwave generators and analyzers.

The significance of new YIG-based spintronic devices originates from the two features of YIG materials: (1) extremely small damping, as mentioned above, and (2) electrically insulating. The intrinsic damping constant α indicated above for YIG is two orders of magnitude smaller than that in transition metals which are the materials of choice in current spintronic devices.

---

[5] M. Wilson, Physics Today, May 2010, page 13.
[6] J. Sinova, Nature Mater. **9**, 880 (2010).
[7] B. Lax and K. J. Button, *Microwave Ferrites and Ferrimagnetics* (McGraw-Hill, New York, 1962).
[8] P. Kabos and V. S. Stalmachov, *Magnetostatic Waves and Their Applications* (Chapman & Hall, London, 1994).
[9] J. D.Adam, L. E. Davis, G. F. Dionne, E. F. Schloemann, and S. N. Stitzer, IEEE Trans. Microwave Theory Tech. **50**, 721 (2002).
[10] D. Stancil and A. Prahakar, *Spin Waves – Theory and Applications* (Springer, New York, 2009).

This small-damping characteristic is highly desirable for many applications, including spin-wave based logic operations and generation of large pure spin currents. Insulator-based spintronic devices are particularly attractive from the engineering point of view. They not only require substantially low power, but also involve no issues that are intrinsically associated with charge currents.

1.2 Dissertation organization

The organization of this dissertation is as follows. Chapter 2 gives an introduction to YIG properties, the spin pumping effect, thin film deposition techniques, and relevant measurement techniques. Chapters 3 and 4 present the growth and FMR properties of low-damping nanometer-thick YIG films. Chapters 5 and 6 demonstrate the experimental results on nanometer-thick YIG based spintronic effects: spin pumping and the magnetic proximity effect. Chapter 7 reports on the successful fabrication of high-quality YIG thin films on metals and their FMR properties. Chapter 8 summarizes the main conclusions and lists future work that is relevant to the topics addressed in this dissertation.

CHAPTER 2

INTRODUCTION TO YIG SPINTRONICS AND THIN FILM GROWTH AND CHARACTERIZATION

2.1 Structure and magnetic properties of YIG

Yttrium iron garnet ($Y_3Fe_5O_{12}$) was discovered by Bertaut and Forrat in 1956.[11,12] It is a prototype of magnetic garnets which are ferrimagnetic oxides and were referred to as "the fruitfly of magnetism" by Kittel.[4] Yttrium iron garnet has nearly cubic symmetry, definite composition, the presence of only trivalent metal ions, and very low magnetic damping. These properties make it particularly suitable for studies of spin waves and magneto-optical effects, as well as for blooming studies of magnetic insulator-based spintronics.

[11] F. Bertaut and F. Forrat, Compt. Rend. **242**, 382 (1956).
[12] S. Geller and M. A. Gilleo, Acta Cryst. **10**, 239 (1957).

The cubic unit cell in yttrium iron garnet has a lattice constant of 12.376±0.004 Å. Each unit cell consists of eight chemical formula units and, thereby, contains twenty-four Y^{3+} ions, forty Fe^{3+} ions, and ninety-six O^{2-} ions.[13,14] The Y^{3+} ions are situated on *c* sites, each site being surrounded by eight O^{2-} ions that form an eight-cornered twelve-sided polyhedron. Of the forty Fe^{3+} ions, sixteen occupy *a* sites and twenty-four occupy *d* sites. The *a* site is also called an octahedral site. It is surrounded by six O^{2-} ions in octahedral symmetry. The *d* site is also called a tetrahedral site and is surrounded by four O^{2-} ions in tetrahedral symmetry. The O^{2-} ions are on *h* sites, each being at a point where the corners of one octahedron, one tetrahedron, and two polyhedrons meet. Thus, each O^{2-} ion is surrounded by one *a*-site Fe^{3+} ion, one *d*-site Fe^{3+} ion, and two *c*-site Y^{3+} ions. Figure 1 shows schematic diagrams for the above-mentioned *c*, *a*, and *d* sites.

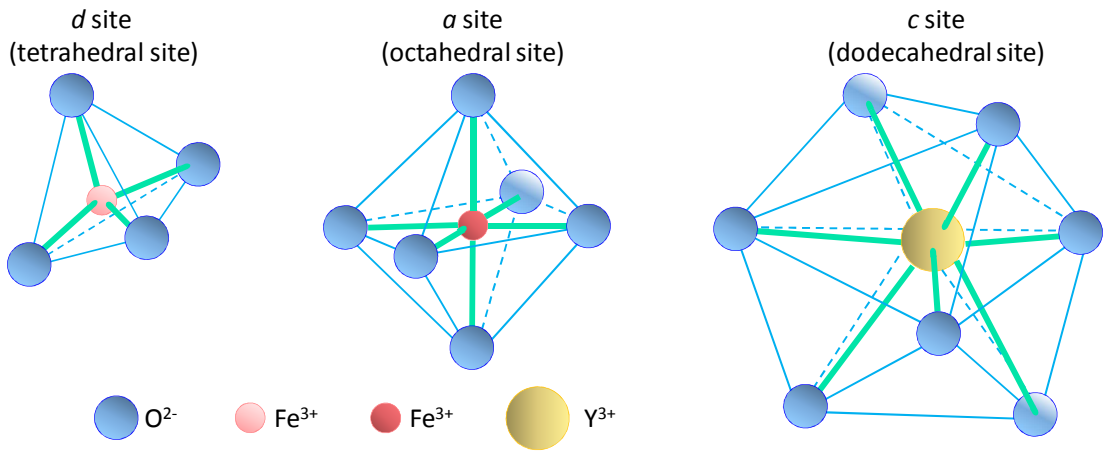

FIG. 1. Schematic diagrams of three different sites occupied by cations in yttrium iron garnet.

[13] M. A. Gilleo and S. Geller, Phys. Rev. **110**, 73 (1958).
[14] G. Winkler, *Magnetic Garnets* (Friedr. Vieweg & Sohn Verlagsgesellschaft mbH, Braunschweig, 1981).

The cation arrangement in a YIG unit cell can be described by a simplified picture shown in Fig. 2.[14] Graph (a) indicates the positions of *a*-site Fe^{3+} ions in front four octants of the YIG unit cell, while graph (b) indicates the positions of the same ions in one octant only. One can see that the *a*-site Fe^{3+} ions in each octant form a body-centered cubic (bcc) sub-unit cell, and the edge of this sub-unit cell is half of the side of the YIG unit cell. Graph (c) indicates the positions of *d*-site Fe^{3+} ions and *c*-site Y^{3+} ions in one sub-unit cell. These ions are on the

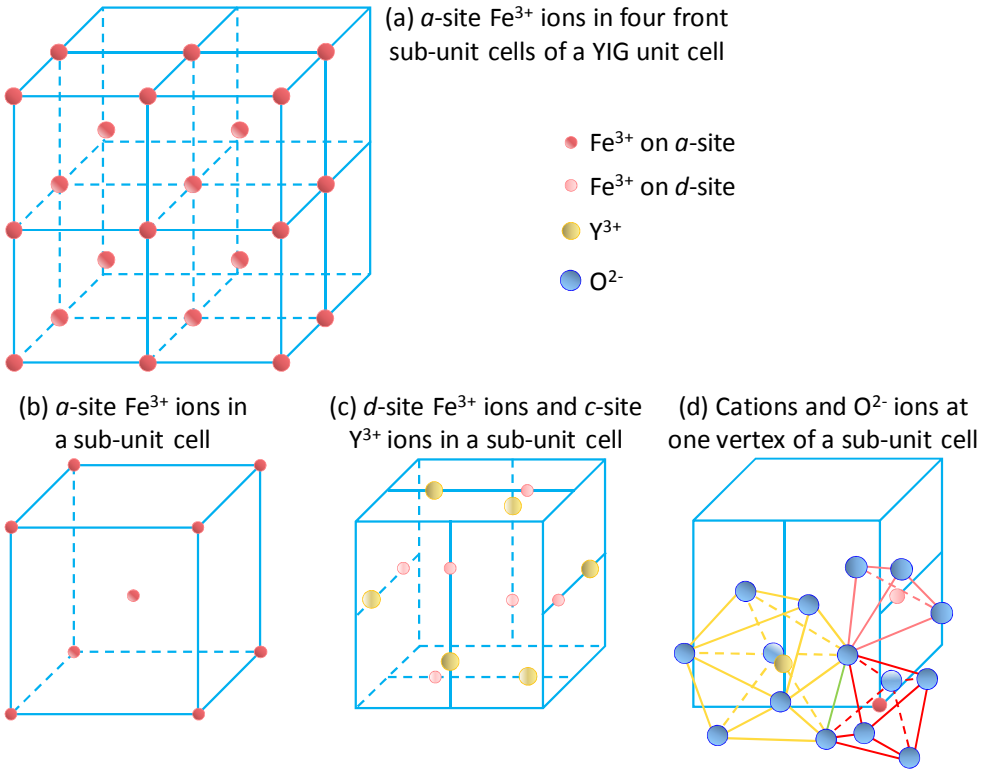

FIG. 2. Cation arrangement in yttrium iron garnet (YIG). One sub-unit cell represents one octant of a cubic unit cell of yttrium iron garnet.

perpendicular bisecting lines of the surfaces of the sub-unit cell, being a quarter from one edge and three quarters from the opposite edge. Graph (d) shows the positions of the *a*-site Fe^{3+} ion, the *d*-site Fe^{3+} ion, and the *c*-site Y^{3+} ion at the front-right-bottom vertex of a sub-unit cell as well as all the O^{2-} ions surrounding them. One can see that the O^{2-} ion at the point where the

three polyhedrons meet is surrounded by the three cations. In fact, this O^{2-} ion is surrounded by four cations. In addition to the three cations shown in graph (d), the fourth cation is the Y^{3+} ion on the bottom surface of the sub-unit cell. This Y^{3+} ion is shown in graph (c), but not in graph (d).

The Y^{3+} ions have no permanent magnetic moment. The magnetization in yttrium iron garnet originates from the super-exchange interactions between the *a*-site Fe^{3+} ions and the *d*-site Fe^{3+} ions. According to the Néel theory, the magnitude of the super-exchange interactions between two magnetic ions depends strongly on the angle of the magnetic ion – oxygen ion – magnetic ion bond. The strongest interactions occur at the bond angle nearest 180°, while the weakest interactions occur for the angle nearest 90°. In yttrium iron garnet, the "*a*-site Fe^{3+}" - O^{2-} - "*d*-side Fe^{3+}" bond has the largest angle, which is 126.6°.[7] Thus, the strongest super-exchange interactions occur between the nearest *a*-site Fe^{3+} and *d*-site Fe^{3+} ions. This interaction results in anti-parallelism between the magnetic moments of the *a*-site Fe^{3+} ions and those of the *d*-site Fe^{3+} ions. Since each Fe^{3+} ion has a magnetic moment of five Bohr magnetons ($5\mu_B$), each unit cell has a net magnetic moment of $40\mu_B$. This magnetic moment corresponds to a theoretical saturation induction $4\pi M_s$ of about 2470 G, which is very close to the value (2463 G) measured for YIG thin films at 4.2 K.[15] The room-temperature $4\pi M_s$ value reported ranges from 1730 G to 1780 G,7 and a widely accepted value is 1750 G. Yttrium iron garnet has cubic magneto-crystalline anisotropy with an easy axis along the (111) direction. The first- and second-order cubic anisotropy constants at room temperature are K_1=-6100 erg/cm^3 and K_2=-260 erg/cm^3, respectively.[10] Yttrium iron garnet thin films are usually grown on (111) gadolinium gallium garnet (GGG) substrates. The difference between the YIG and

[15] H. A. Algra and P. Hansen, Appl. Phys. A **29**, 83 (1982).

GGG lattice constants is extremely small, on the order of 0.001 Å. A (111) YIG film has an out-of-plane effective anisotropy field ($2K_1/M_s$) of about 85 Oe and a threefold in-plane effective anisotropy field of less than 85 Oe. These fields are much smaller than the external magnetic fields used in typical experiments and, therefore, are usually ignored in data analysis.

In YIG Crystal, the ferromagnetic resonance (FMR) linewidth originated from intrinsic damping in YIG crystals is about 0.2 Oe at 10 GHz.[16,17] This linewidth corresponds to an intrinsic Gilbert damping constant α of about 3×10^{-5}, which is about one order of magnitude smaller than that in barium hexagonal ferrites[18] and about two orders of magnitude smaller than that in ferromagnetic metals.[19,20] It is this extremely small damping constant that makes yttrium iron garnet the material of choice for studies of spin waves as well as magnetic insulator-based spintronics.

Table I gives some structural and physical properties of single-crystal yttrium iron garnet. The values listed (except the Curie temperature) are measured at room temperature, unless a particular temperature is specified.

Table I. Properties of yttrium iron garnet

Parameter	**Value**	**Reference**
Lattice constant *a* (273 K)	12.376±0.004 Å	14, 7
Lattice constant *a* (77 K)	12.361 Å	14
Lattice constant *a* (4 K)	12.359 Å	14
Thermal expansion coefficient (298 K)	8.3×10^{-6}	14

[16] M. Sparks, *Ferromagnetic-Relaxation Theory* (McGraw Hill, New York, 1964).
[17] A. G. Gurevich and G. A. Melkov, *Magnetization Oscillations* (CRC Press, Boca Raton, 2000).
[18] Y. Y. Song, S. Kalarickal, and C. E. Patton, J. Appl. Phys. **94**, 5103 (2003).
[19] Z. Celinski and B. Heinrich, J. Appl. Phys. **70**, 5935 (1991).
[20] S. S. Kalarickal, P. Krivosik, M. Wu, C. E. Patton, M. L. Schneider, P. Kabos, T. J. Silva, and J. P. Nibarger, J. Appl. Phys. **99**, 093909 (2006).

Thermal expansion coefficient (623 K)	11.0×10^{-6}	14
Density	5.17 g/cm^{-3}	10
Band gap	2.85 eV	10
Saturation induction $4\pi M_s$	1750 G	7
Saturation induction $4\pi M_s$ (4.2 K)	2463 G	15
Cubic anisotropy constant K_1	-6100 erg/cm^3	10
Cubic anisotropy constant K_2	-260 erg/cm^3	10
Curie temperature T_c	559 K	10
Exchange constant α	3×10^{-12} cm^2	10
Intrinsic damping constant α	3×10^{-5}	16
Faraday rotation (1.2 μm)	240 deg/cm	10
Dielectric constant (10 GHz)	14.7	21
Dielectric loss tangent (10 GHz)	0.0002	21

2.2 **Spin Pumping**

Figure 3 illustrates the spin pumping effect in a ferromagnetic (FM)/normal metal (NM) bilayer structure. The arrow in the FM layer shows a unit vector $\hat{\mathbf{m}}$ which denotes the direction of the magnetization. The bottom diagrams show simplified band structures. The vertical arrows indicate the directions of electron magnetic moments. When the magnetization in the FM layer is static, the electrons in the two layers share the same Fermi level. When the magnetization is excited to precess, the FM layer passes a certain net angular momentum to the NM layer. The net effects are a difference between the chemical potentials of spin-up electrons ($\mu_\uparrow$) and spin-down electrons ($\mu_\downarrow$) and a spin current in the NM layer. This effect is called spin

[21] H. How, P. Shi, C. Vittoria, L. C. Kempel, and K. D. Trott, J. Appl. Phys. **87**, 4966 (2000).

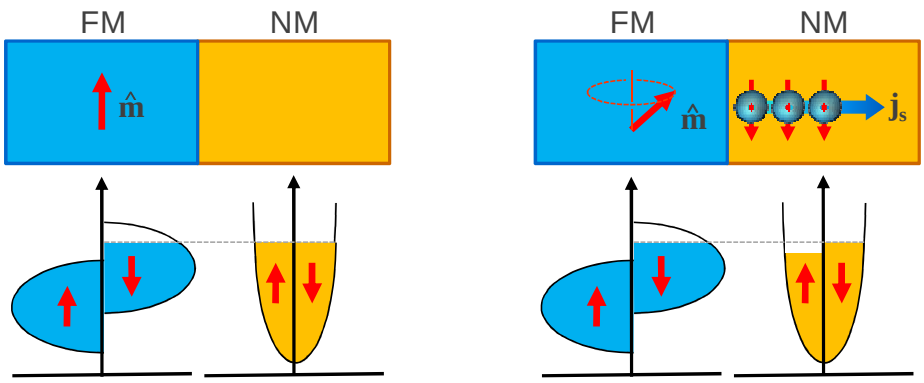

FIG. 3. Spin pumping in a ferromagnetic (FM)/normal metal (NM) bilayer structure.

pumping.[22,23] Note that the small spheres in the NM layer represent electrons and the arrow through each sphere indicates the direction of the electron magnetic moment. Note also that the chemical potential difference $\mu=\mu_{\uparrow}-\mu_{\downarrow}$ is often called a spin voltage or a spin accumulation.

One often considers a spin current density vector

$$\mathbf{J}_s = \frac{\hbar}{4\pi}\mathrm{Re}\left(g_{\uparrow\downarrow}\right)\hat{\mathbf{m}}\times\frac{\partial\hat{\mathbf{m}}}{\partial t} \tag{2.1}$$

where $g_{\uparrow\downarrow}$ denotes the spin mixing conductance across the FM/NM interface. This density is indeed the net angular momentum transferred from to the spins in the FM layer to the electrons in the NM layer through a unit interface area within a unit time. This momentum transfer results in an increase in the damping constant α in the FM layer, which can be written as

$$\alpha_{sp} = \frac{g\mu_B}{4\pi M_s}\frac{\mathrm{Re}\left(g_{\uparrow\downarrow}\right)}{d} \tag{2.2}$$

[22] Y. Tserkovnyak, A. Brataas, and G. E. W. Bauer, Phys. Rev. B **66**, 224403 (2002).
[23] B. Heinrich and J. A. C. Bland, *Ultrathin Magnetic Structures: Fundamentals of Nanomagnetism* (Springer, Berlin, 2005).

where μ_B is the Bohr magnetron, and g, $4\pi M_s$, and d are the Landé factor, saturation induction, and thickness, respectively, of the FM layer.

2.3 Thin film deposition systems

2.3.1 Pulsed laser deposition

Pulsed laser deposition (PLD) is one kind of high vacuum physical vapor deposition (PVD) technique. The target materials with complex components can be ablated by the laser and deposited stoichoimetrically on the substrates. That means the deposited thin films have the exact same components as those of the targets. Due to this advantage, the PLD technique has been widely used in the deposition of complex compounds, such as garnets, ferrites, and superconductor materials.

Figure 4 shows a schematic diagram of the PLD system, by which the YIG films reported in this dissertation were prepared. The main components include a pulsed laser source, a high vacuum chamber, a rotatable target holder, and a substrate holder with a built-in heater (not rotatable). The pulsed laser beam is reflected and converged by a series of mirrors and lenses and strikes on the target inside the chamber. Because of the high power of the laser, the target material is evaporated and forms the plume normal to the target. The plume has complicated components of electrons, ions, evaporated atoms molecules, and clusters. The plume then crosses the vacuum to the substrate and the thin film is formed. Prior to the deposition, the base pressure in the chamber is 2.7×10^{-7} Torr, which is realized by using the cascaded mechanical-turbo molecular pumps and through a high temperature baking process. During the deposition, the chamber can either keep high vacuum or be filled with other reactive gases such

as oxygen. The substrate holder integrated with temperature control can heat the substrate and increase its temperature to be as high as 900 °C. The optimization of deposition temperature is the most critical factor to grow high-quality YIG thin films by PLD. The other important parameters include the laser power, repetition rate, oxygen pressure, cooling rate, and post-annealing parameters. The details of the PLD deposition will be presented in Chapters 3 and 7.

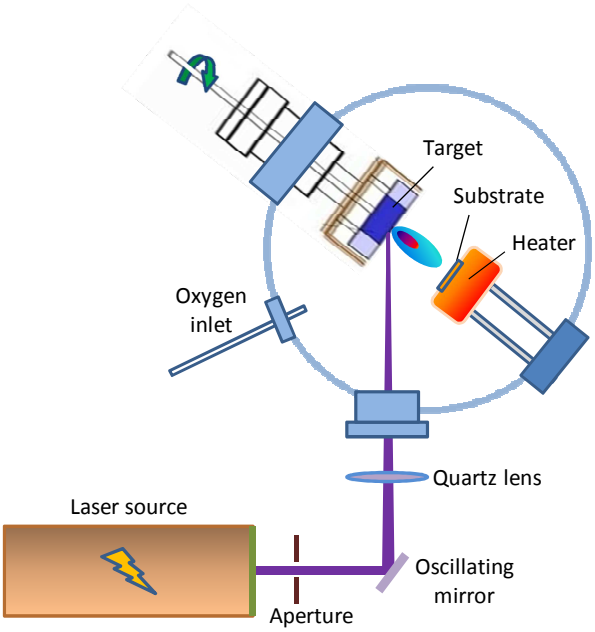

FIG. 4. Schematic diagrams of pulsed laser deposition system.

2.3.2 Magnetron sputtering

Magnetron sputtering is another widely used PVD technique. Because the sputtered thin films have relatively high uniformity, the magnetron sputtering technique is favorable for use in the semiconductor, optics, magnetic storage, and other industries.

During the sputtering process, argon (Ar) is backfilled into the growth chamber and the Ar atoms are ionized by a high voltage of several kilo volts. In the system, the magnets under the

target can trap the free electrons and enhance the ionization efficiency of the Ar atoms. After acceleration by strong magnetic and electric fields, the Ar^+ ions strike on the surface of the target and transfer their kinetic energy into thermal energy in the target materials. The net effect is the neutral particles such as individual atoms and clusters of atoms or molecules are ejected from the target and fly straight toward the substrate. The substrate then will be coated by the thin

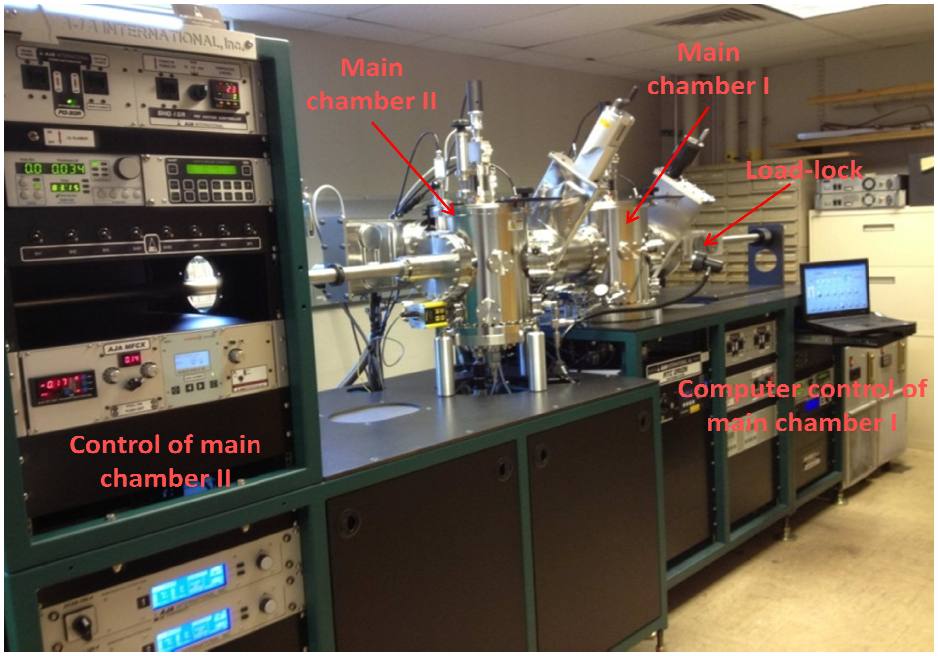

FIG. 5. Picture of the CSU magnetron sputtering system.

films of the target materials. To improve the thin film uniformity, the substrate holder rotates during the sputtering process.

Our laboratory has a three-chamber magnetron sputtering system as shown in Figure 5. The three chambers, respectively from right to left, are used to load samples, sputter metallic thin films, and deposit oxide materials. Crystal oscillator thickness monitors were installed in the growth champers to precisely measure the growth rate. In this dissertation, some of the capping layers of the YIG films were fabricated by the magnetron sputtering system. The

sputtering system was also used to do the low power etching to remove the defects on the surface of YIG nano films. The details will be provided in Chapters 4 and 7.

2.4 Measurements techniques

The correlations between microstructures and magnetic properties are always critical topics of study for magnetic thin films. The characterizations of the structure and magnetic properties along with the correlation studies give important information on how to improve the quality of the thin film. In this dissertation, thin film X-ray diffraction (XRD), scanning electron microscopy (SEM), and atomic force microscopy (AFM) were used to characterize the samples' structures. X-ray photoelectron spectroscopy (XPS) and energy dispersive spectroscopy (EDS) were applied to measure the samples' compositions. The static magnetic properties were characterized by a superconductor quantum interference device (SQUID) system. The magnetization dynamics was studied by using ferromagnetic resonance (FMR) techniques.

2.4.1 Structure characterizations

High-quality YIG thin films are required for both microwave and spintronics applications, as mentioned in Chapter 1. "High-quality" means a good crystalline structure, which results in the low damping in YIG. Ideally, perfect single-crystal YIG bulks have the lowest damping of 3×10^{-5}. If the quality of the crystalline structure declines, the microwave loss increases and the damping constant increases by a factor of 10 to 100. Therefore, the magnetic damping can be reflected by the quality of the crystalline structure which is generally determined by XRD techniques. Two XRD testing modes are demonstrated in this dissertation. One is the 2-θ scan, which gives the information about the crystal orientation, grain size, and even strain/stress

in the lattice. The other is the rocking-curve mode, in which the full width at the half maximum (FWHM) tells the quality of the crystal, i.e. the narrower FWHM means higher quality.

Figure 6 shows a typical XRD 2-θ scan for our nanometer-thick YIG films. Using a large angle range (20 to 90 degrees), only the (222), (444), and (666) diffraction peaks can be observed. This indicates the YIG layer was epitaxially grown along the (111) direction of the single-crystal GGG substrate. There is no other phase detected in this range. The inset shows the rocking curve of the strongest peak (444). The rocking curve measurements show two results: (1) the clear separation of the YIG (444) peak from the GGG (444) peak and (2) the FWHM of the YIG (444) is as narrow as that of the GGG (444) peak.

These two points together indicate the highly crystallized structure of the YIG film.SEM measurements can give both the surface topography and cross-section images of the testing film samples. The former provides the information related to the film's uniformity, continuity, grain

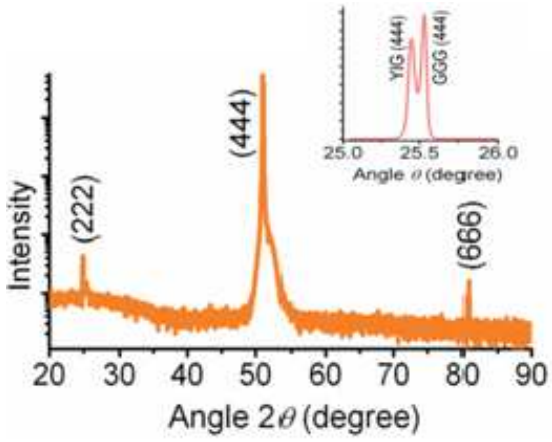

FIG. 6. XRD 2-θ scan and rocking-curve (inset) for a typical YIG thin film.

size, and even the crystal structure. The latter always tells the thickness of each layer, interlayer diffusion, and also the crystal structure. As another surface topography characterization tool, AFM is generally used to obtain the surface roughness of the film samples. In addition, the uniformity, continuity, and grain size properties can also be characterized or measured by using the AFM technique.

Taking the YIG/HCH/GGG[24] sample as an example, its multilayer structure can be observed clearly in Figure 7(a) through the SEM cross-section measurement. Figure 7(c) shows the SEM surface image of the same sample, which indicates the film having very dense nano grains. Figure 7(d) shows the AFM surface image, and both the roughness and grain size can be calculated by the statistics software integrated in the AFM system. Note that "HCH" in this sample refers to a layered HEAN/Cu/HEAN structure where HEAN denotes high entropy alloy nitrides.

EDS and XPS are the most common tools of elements analysis. They have similar

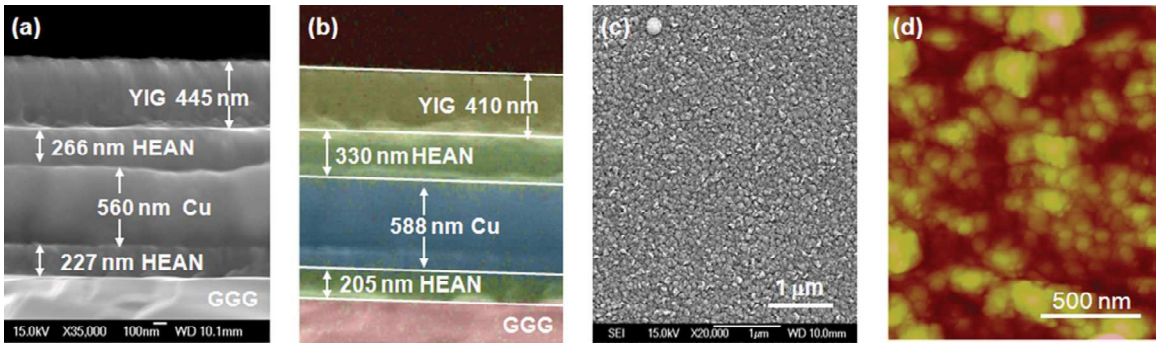

FIG. 7. (a) Cross-section SEM, (b) cross-section EDS, (c) surface SEM, and (d) surface AFM images of a YIG/HEAN/Cu/HEAN sample.

[24] Y. Sun, Y.-Y. Song, and M. Wu, Appl. Phys. Lett. **101**, 082405 (2012).

principles. As a beam of high energy electrons strikes the sample, an X-ray is excited and detected. The EDS is usually integrated with the SEM and shares the same electron beam. Figure 7(b) shows the EDS result for the same area of the sample measured by SEM (see Figure 7(a)). Different colors stand for different components. Through the comparison of Figures 7(a) and 7(b), one can check the interfacial diffusion and find out the actual layer-to-layer boundaries.

Figure 8 shows one typical XPS result for our nano YIG films. Different elements or the same element with different states have their own unique XPS peaks. These peaks can be characterized by the bonding energy. In other words, the elemental composition, chemical state,

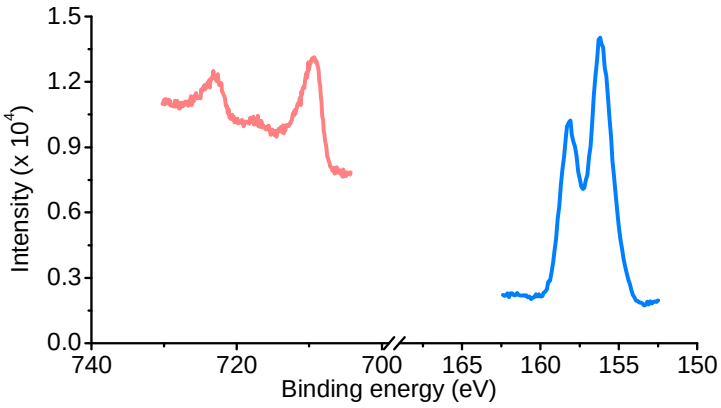

FIG. 8. XPS spectrum of Fe and Y in a YIG sample

and electronic state can all be determined by the bonding energy of the XPS characteristic peaks. The atom ratio measurement is another important function of the XPS technique. In Figure 8, for example, the area under the double-peak on the left side gives the relative amount of Fe atoms, while the area under the peaks on the right side gives the amount of Y atoms. Therefore, the atom ratio is actually equal to the ratio of the areas. The details about the atom ratio analysis by XPS are presented in Chapters 3 and 4.

2.4.2 Measurements of static magnetism

As a ferrimagnetic material, YIG has the saturation induction ($4\pi M_S$) of 1750 G. Because the GGG substrate is a paramagnetic material, the *M-H* measurements of YIG/GGG actually give the overall magnetic signals from both the ferrimagnetic YIG and the paramagnetic GGG. In theory, the ferrimagnetic material has hysteresis behavior in the *M-H* measurement, while paramagnetic materials show a linear response. When the thickness of YIG is reduced to the nanometer scale, the magnetic moment of the YIG layer can be as low as 10^{-5} emu if the sample's in-plane dimension is in the millimeter scale. This makes the substrate magnetic moment have the dominant contribution to the overall signal, which leads to the measured YIG/GGG *M-H* loop having an obvious linear response. To obtain the hysteresis loop of a YIG layer, the substrate's paramagnetic contribution needs to be removed by subtracting the slope of the data measured at the high field range. The high field should be far beyond the YIG's saturation field. Because of its superconductor loop, SQUID has very high sensitivity in comparison to other static magnetic measurement equipment such as a vibrating sample magnetometer (VSM) and an *M-H* looper. SQUID can also be used for temperature-dependent magnetization and electrical transportation measurements. The SQUID measurement temperature can be as low as the temperature of liquid helium temperature at 4 Kelvin.

Figure 9 shows the *M-H* loop before and after subtracting the substrate contribution. The graph on the right side is a typical hysteresis loop of nanometer-thick YIG films. Such samples have a very small coercivity and a very small saturation field. The saturation induction can be calculated through dividing the saturated magnetic moment by the volume of the film. For our nanometer-thick YIG films, the saturation induction is about 1300 G.

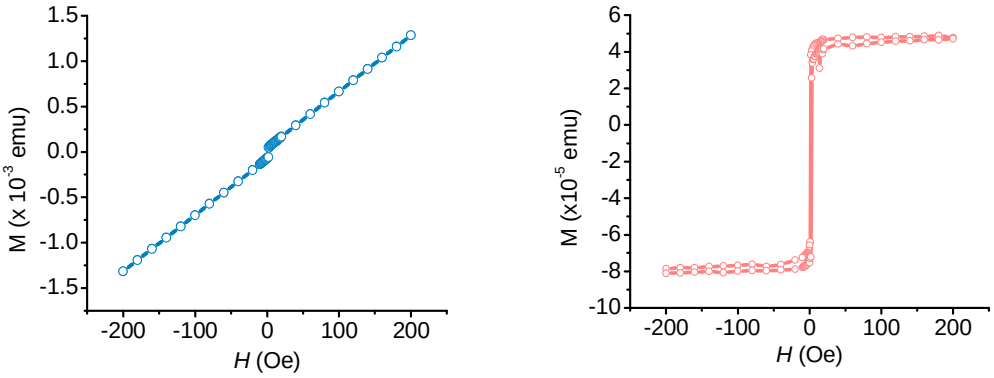

FIG. 9. *M-H* loop of a YIG/GGG sample measured by SQUID. Left: the measured response. Right: the *M-H* loop after the removal of the paramagnetic contribution.

2.4.3 Ferromagnetic resonance

In magnetic materials, a torque exists if the magnetization has a different direction from the external magnetic field. This torque will result in the magnetization precession. If the angle doesn't change during the precession, it is called uniform precession. However, in the real materials, the interactions of magnon-phonon, magnon-electron, and magnon-magnon will damp the precession. Without a driving force, the precession angle will be reduced with time and finally become zero. Such types of processes are called magnetization relaxation. The research field of magnetization dynamics is mainly related to the study of the damping mechanism, relaxation time, spin transfer torque, domain wall motion, and magnetization switching, and so on. Ferromagnetic resonance is widely used to study the magnetization dynamics. The measurement of the FMR response not only gives the values of the magnetization dynamic quantities of the material like the damping and the relaxation rate, but also tells the information about the static magnetic properties including the saturation induction and the anisotropy field. In the following, the FMR technique is introduced in detail.

One of the main issues related to the magnetic insulator-based spintronics is the mutual interaction between spin currents and magnetization precession. A spin current can influence the magnetization precession through the angular momentum transfer at the magnetic insulator (MI)/normal metal (NM) interface. This is realized either by the interfacial spin scattering or by spin pumping. The FMR technique is the direct method to test the damping and determine the efficiency of angular momentum transfer quantitatively.

As mentioned above, FMR is the most typical technique to study the magnetization dynamics. If there is some kind of driving force that overcomes the damping, as shown in Figure 10 (a), the magnetization can process without a reduction in the precession angle. This is called driving precession. In the FMR system, the driving force is in the form of a microwave magnetic field, whose direction is perpendicular to the external magnetic field. The magnetization dynamics can be described by the Gilbert equation,

$$\frac{d\mathbf{M}}{dt} = -|\gamma|\mathbf{M}\times\mathbf{H} + \frac{\alpha}{M_s}\mathbf{M}\times\frac{d\mathbf{M}}{dt} \tag{2.3}$$

where α is the damping constant and its value can be determined by FMR measurements. There are two kinds of FMR scan modes: the field scan and the frequency scan. The former is done at a fixed microwave frequency with the magnetic field changes continuously, while the latter makes the magnetic field constant and the frequency changes. Whatever the scan mode is, once the field/frequency meets the resonance condition, the material under test will have the maximum power absorption. For example, the FMR system shown in Figure 10(b) has the field scan mode. During the measurements, the sample is put into the cavity or the shorted waveguide. These are located in the center of the magnetic field. Then microwaves are sent out

by the microwave generator and propagate along the waveguide to reach the sample. The lock-in amplifier and modulation field are also used for the measurements. Figure 10(c) shows a representative FMR profile measured by the filed scan mode. The y-axis refers to the absorption derivative, which is the first-order derivative of the power absorption. The difference between the peak and dip of the profile is defined as the peak-to-peak linewidth. In this dissertation, all the linewidths are referring to the peak-to-peak linewidths. Generally, the FMR linewidth increases with the microwave frequency. The relationship between the FMR linewith and the frequency has a linear response in some cases as shown in Figure 10(d), and is therefore described by a linear equation

$$\Delta H_{\mathrm{FMR}} = \Delta H_0 + \frac{1}{\sqrt{3}} \frac{2\alpha}{|\gamma|} \frac{\omega}{2\pi} \tag{2.4}$$

The Gilbert damping constant is proportional to the slope of the straight line, i.e. a steeper slope indicates a larger damping constant. The discussion above indicates that the frequency-dependent FMR measurements will give the Gilbert damping values of the samples.

In the spin pumping experiments, the damping of a magnetic insulator (MI) is enhanced because the angular momentum transfers out of the magnetic layer. The interfacial spin scattering has two situations regarding the damping change. (1) If the spin current's polarization is parallel to the magnetization of the MI, the induced torque counters the damping. (2) If the polarization is anti-parallel to the magnetization, the torque increases the damping.

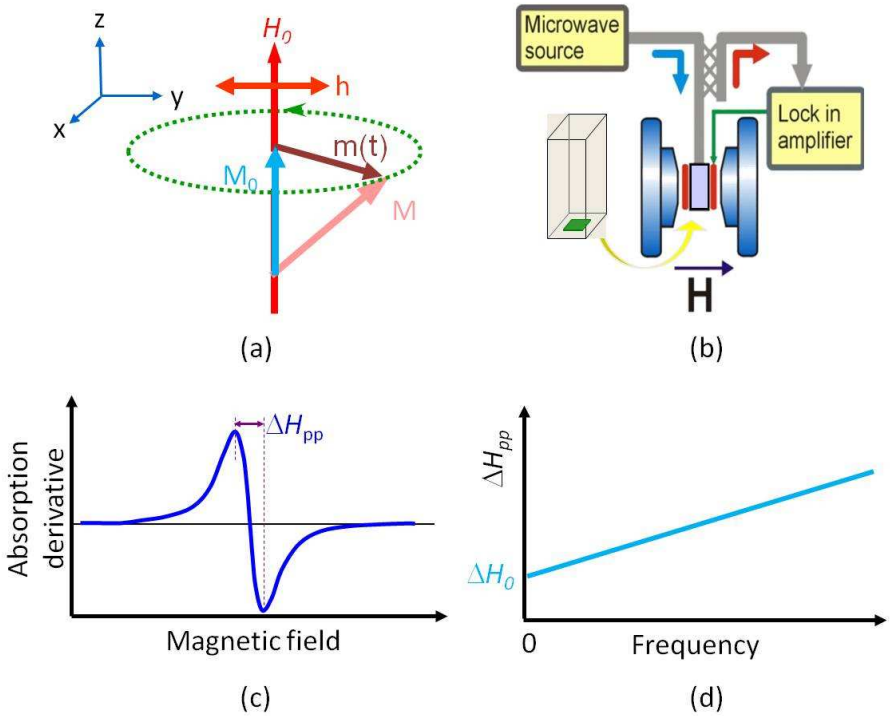

FIG. 10. (a) Schematic diagram of magnetization precession. (b) Schematic diagram of an FMR system. (c) A representative FMR profile. (d) Linear response of frequency-dependent FMR linewidth.

CHAPTER 3

GROWTH OF YIG NANO FILMS

3.1 Overview of YIG growth

It is known that liquid phase epitaxy (LPE) is the best technique for the growth of micron-thick YIG films,[25,26,27] while PLD and radio-frequency (RF) sputtering are the techniques of choice for the deposition of submicron-thick films.[28,29,30,31,32,33,34,35,36] It is also possible to use PLD techniques to grow micron-thick YIG films with very narrow linewidth (for example, about 1 Oe at 9.5 GHz).[28,36] These films, however, show effective anisotropy fields one order of magnitude larger than those of LPE films. The realization of high-quality YIG films usually requires the use of high temperature (700-900 °C). However, there are also reports where one deposits YIG films via sputtering at room temperature first and then makes use of high-temperature annealing to improve the quality of the films.[35]

---

[25] R. C. LeCraw, E. G. Spencer, C. S. Porter, Phys. Review, **110**, 1311 (1958).
[26] R. C. Linares, R. B. McGraw, and J. B. Schroeder, J. Appl. Phys. **36**, 2884 (1965).
[27] M. Shone, Circuits Systems Signal Process. **4**, 89 (1985).
[28] P. C. Dorsey, S. E. Bushnell, R. G. Seed, and C. Vittoria, J. Appl. Phys. **74**, 1242 (1993).
[29] M.-B. Park, B. J. Kim, and N.-H. Cho, IEEE Trans. Magn. **35**, 3049 (1999).
[30] Y. Krockenberger, K.-S. Yun, T. Hatano, S. Arisawa, M. Kawasaki, and Y. Tokura, J. Appl. Phys. **106,** 123911 (2009).
[31] S. A. Manuilov and A. M. Grishin, J. Appl. Phys. **108,** 013902 (2010).
[32] T. Boudiar, S. Capraro, T. Rouiller, M.-F. Blanc-Mignon, B. Payet-Gervy, M. Le Berre, and J.-J. Rousseau, Phys. Stat. Sol. (C) **1,** 3347 (2004).
[33] S. Yamamoto, H. Kuniki, H. Kurisu, M. Matsuura, and P. Jang, Phys. Stat. Sol. (A) **201,** 1810 (2004).
[34] S.- Y. Sung, X. Qi, and B. J. H. Stadler, Appl. Phys. Lett. **87**, 121111 (2005).
[35] Y.-M. Kang, S.-H. Wee, S.-I. Baik, S.-G. Min, S.-C. Yu, S.-H. Moon, Y.-W. Kim, and S.-I. Yoo, J. Appl. Phys. **97**,10A319 (2005).
[36] S. A. Manuilov, R. Fors, S. I. Khartsev, and A. M. Grishin, J. Appl. Phys. **105**, 033917 (2009).

In contrast to considerable previous work on the growth of micron- or submicron-thick YIG films, little work has been carried out on the growth of nm-thick YIG films so far. There are two reports on the realization of YIG nano films by PLD techniques.[37,38] Reference [37] focused on the thickness dependence of the structure and magnetization of PLD YIG nano films but provided no information on the damping of the films. In Ref. [38], the PLD YIG nano films showed a peak-to-peak FMR linewidth of about 300 Oe, which is three orders of magnitude lager than those in bulk YIG crystals.

3.2 **High-quality YIG nano films deposited by PLD**

This chapter presents experimental results that demonstrate the feasibility of the growth of high-quality YIG nano films by PLD techniques with optimized control parameters.[39] The deposition used (111) GGG substrates. The films with a thickness between 5-35 nm exhibited a (111) orientation and showed a surface roughness in the range of 0.1-0.3 nm. The 10-nm-thick films showed an FMR linewidth of about 6 Oe at 10 GHz and a damping constant of about 3.2×10^{-4}. This linewidth is 50 times smaller than that reported previously for the YIG films of similar thicknesses.[38] The damping constant is only one order of magnitude larger than the intrinsic value of YIG crystals (see Table I) and is one to two orders of magnitude smaller than that of ferromagnetic metallic nano films.[19,20]

[37] N. Kumar, D. S. Misra, N. Venkataramani, S. Prasad, and R. Krishnan, J. Magn. Magn. Mater. **272-276,** e899 (2004).

[38] E. Popova, N. Keller, F. Gendron, M. Guyot, M.-C. Brianso, Y. Dumond, and M. Tessier, J. Appl. Phys. **90,** 1422 (2001).

[39] Y. Sun, Y.-Y. Song, H. Chang, M. Kabatek, M. Jantz, W. Schneier, M. Wu, H. Schultheiss, and A. Hoffmann, Appl. Phys. Lett. **101**, 152405 (2012).

For the YIG films discussed in this dissertation, the deposition used 248 nm KrF excimer laser pulses with a duration of 30 ns, 1-inch-diameter YIG targets, and 0.5-mm-thick single-crystal (111) GGG substrates. The deposition was carried out in a high-purity oxygen atmosphere (99.999%). Prior to the deposition, the system had a base pressure of 3.4×10^{-7} Torr. To a large extent, the film quality depends on the deposition and post-deposition annealing control parameters. These parameters were optimized for the growth of small-linewidth films with thicknesses of 5-35 nm. For the data presented below, the films were prepared with the following control parameters. (1) The target-to-substrate distance was 7.0 cm. (2) During the deposition, the substrate temperature was 790 °C or 850 °C, the oxygen pressure was fixed at 0.1 Torr, and the laser pulses had an energy fluence of 1.7 J/cm^2 and a repetition rate of 1 Hz or 2 Hz. (3) Immediately after the deposition, the film was annealed at the deposition temperature for 10 minutes with the oxygen pressure increased gradually from 0.1 Torr to 400 Torr. (4) Cooling of the system was carried out in 400 Torr oxygen at a rate of -2 °C per minute.

The morphological and structural properties of the YIG nano films were analyzed through scanning electron microscopy (SEM), x-ray diffraction (XRD), x-ray reflectivity (XRR), x-ray photoelectron spectroscopy (XPS), and atomic force microscopy (AFM) measurements. The field-swept FMR responses were measured by microwave rectangular cavities and shorted waveguides with field modulation and lock-in detection techniques. The YIG film samples were about 2×2 mm squares. The external magnetic fields were applied in the plane of the films. Unless otherwise specified, the FMR linewidth (ΔH_{FMR}) values in this chapter all refer to the peak-to-peak linewidths of FMR power absorption derivative profiles. The ΔH_{FMR} values measured by cavities were consistent with those measured by shorted waveguides.

Figure 11 shows representative data that demonstrate the effects of the substrate temperature T_s and the laser pulse repetition rate f_L during the PLD process. For the data in each column, the films were deposited at the same T_s and f_L parameters. From column to column, the films were deposited at either a different T_s or a different f_L. In each column, the top graph presents an AFM image of the film surface, while the bottom graph presents an FMR profile. In all the FMR profile graphs in this chapter and next chapter, the circles show the FMR data obtained at 9.5 GHz, the curves show Lorentzian fits, and the arrows indicate the linewidths obtained from the fits. The linewidth uncertainties cited were obtained from the Lorentzian fitting.

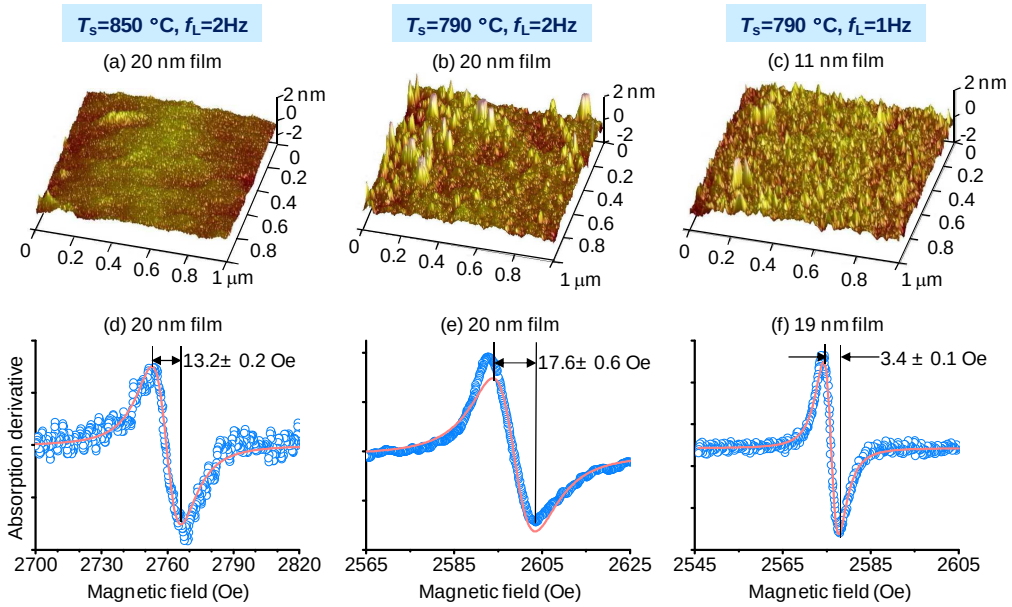

FIG. 11. Effects of substrate temperature T_s and laser pulse repetition rate f_L on the quality of PLD YIG nano films. The first row shows surface AFM images. The second row shows 9.5 GHz FMR power absorption derivative profiles.

The comparison between the images in graphs (a) and (b) indicates that the higher T_s is favorable for the realization of films with smoother surfaces, and the comparison between (b) and (c) suggests that the lower f_L is favorable. Specifically, the surface roughness values for

the films cited in graphs (a), (b), and (c) are 0.16±0.04 nm, 0.32±0.10 nm, and 0.22±0.01 nm, respectively. Note that all roughness values cited in this chapter are averages over the measurements on five different 1μm×1μm areas, and the uncertainties are the corresponding standard deviations. The comparison of the data shown in graphs (d)-(f) suggests that the higher the T_s and the lower the f_L are, the smaller the FMR linewidth is. The reason for this result is discussed in Chapter 4.

The XPS spectra for the films cited in Figs. 11 (a)-(c) are given in Fig. 12. The peaks at lower binding energy are for Y^{3+} ions, while those at higher energy are for Fe^{3+} ions. One can see that these spectra differ from each other. A quantitative analysis on the XPS data yields Y:Fe=3.0:2.1 for the "790 °C, 2 Hz" film, Y:Fe=3.0:2.3 for the "850 °C, 2 Hz" film, and Y:Fe=3.0:2.6 for the "790 °C, 1 Hz" film, which all differ from the expected ratio Y:Fe=3.0:5.0. The ratio Y:O, however, equals 3.0:11.7 for all three films, which almost matches the expected

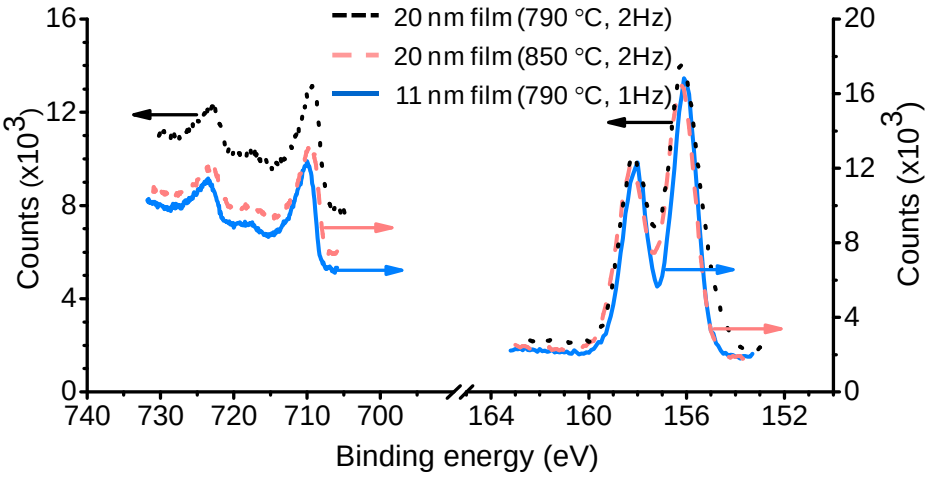

FIG. 12. XPS profiles for PLD YIG nano films grown at different substrate temperatures and laser pulse repetition rates, as indicated.

ratio Y:O=3.0:12.0. These results indicate that there is a deficiency in Fe on the YIG film surface, and this deficiency is smaller if a higher T_s or a lower f_L is used during the deposition.

Figure 13 shows data for an 11-nm-thick YIG film deposited at T_s =850 °C and f_L =1 Hz, which are the highest T_s and the lowest f_L available in our laboratory. Graphs (a) and (b) show the XRD spectra for a (111) GGG substrate alone and for the YIG sample, respectively. The comparison between the two spectra confirms the existence of the YIG phase in the sample and does not indicate the existence of any additional phases. Graph (c) shows a spectrum with an expanded angle scale. This spectrum indicates that the YIG film has (111) orientation, as expected. The polar graph in (d) shows the angle dependence of the FMR field measured with rotating the external magnetic field in the plane of the YIG film. The data indicate that the film

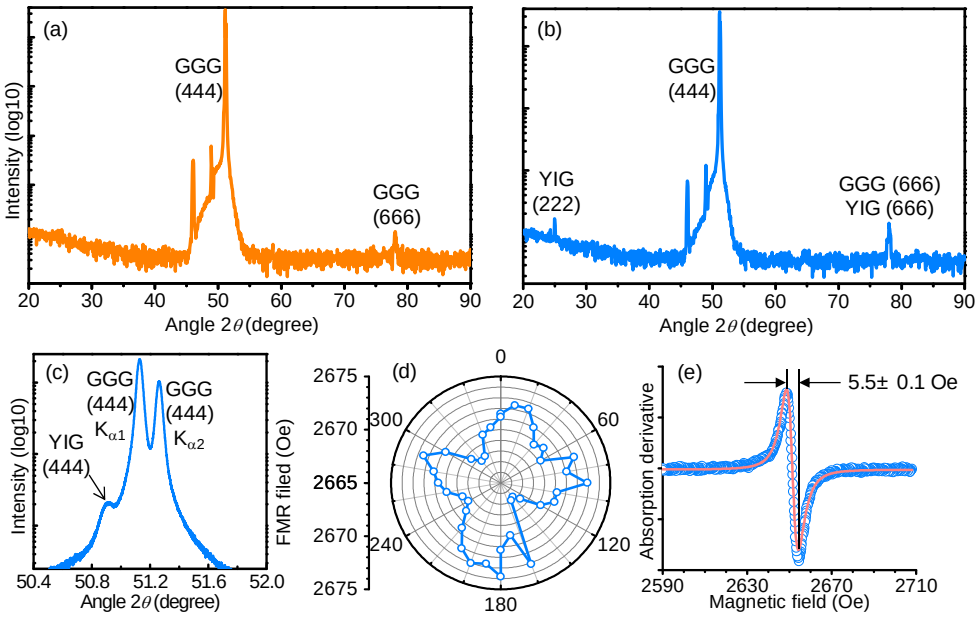

FIG. 13. (a) XRD spectrum of a (111) GGG substrate. (b) and (c) XRD spectra of an 11-nm-thick YIG film. (d) and (e) FMR data for the same YIG film. The polar graph in (d) shows the angle-dependent FMR field. In (e), the circles show the FMR profile and the curve shows a Lorentzian fit. The FMR measurements were carried out at 9.5 GHz with in-plane external fields.

has rather weak in-plane anisotropy with an effective anisotropy field in the 0-7 Oe range. This field is much smaller than the value for single-crystal (111) YIG films, which is mentioned in Chapter 2. One can expect two types of in-plane anisotropy in the YIG film: (i) three-fold magneto-crystalline anisotropy in correspondence with the (111) orientation and (ii) two-fold anisotropy due to the fact that in the PLD process the plasma plume axis has a small angle (about 10º) with the normal direction of the GGG substrate. The anisotropy shown in graph (d), however, is neither three-fold nor two-fold. This may suggest the coexistence of both types of the anisotropy. Graph (e) shows the 9.5 GHz FMR profile. The linewidth indicated is smaller than those of other films of similar thickness deposited at either a lower T_s or a higher f_L.

The above-discussed results together with additional results not presented here indicate three important points. (1) The PLD techniques can be used to grow high-quality YIG nano films. As indicated by the AFM images in Fig. 11, the YIG films show smooth surfaces, with a surface roughness range of 0.1-0.3 nm. Such smooth surfaces will allow for the realization of good interfaces in nano YIG film-based multilayered heterostructures. As indicated in Fig. 11(f) and Fig. 13(e), the YIG nano films show FMR linewidths much narrower than that of ferromagnetic metallic films of similar thickness.[19,20] This demonstrates the advantages of YIG nano films over ferromagnetic metallic nano films in terms of spintronics applications. For spin-torque nano-oscillators, for example, films with small damping are desired for the realization of low threshold currents and narrow spectral linewidths.[40,41,42] (2) Higher T_s and lower f_L values are desirable during the deposition in order to realize high film quality. High

[40] D. C. Ralph and M. D. Stiles, J. Magn. Magn. Mater. **320**, 1190 (2008).
[41] S. Bonetti, V. Teberkevich, G. Cansolo, G. Finocchio, P. Muduli, F. Mancoff, A. Slavin, and J. Åkerman, Phys. Rev. Lett. **105**, 217204 (2010).
[42] K. Mizushima, K. Kudo, T. Nagasawa, and R. Sato, J. Phys.: Conf. Seri. **266**, 012060 (2011).

temperature helps the film crystallization, while low laser repetition rate allows for slow growth. As a result, they are both beneficial for the growth of high-quality films. (3) There is a correlation of the FMR linewidth with the surface roughness and the deficiency of Fe on the film surface. Specifically, the linewidth increases with both surface roughness and Fe deficiency. The underlying physical mechanism for this correlation is discussed in Chapter 4.

3.3 **Summary**

In summary, this chapter demonstrates the feasibility of PLD growth of narrow FMR linewidth YIG nano films and reveals the FMR linewidth properties in such films. High substrate temperature and low laser pulse repetition rate are desired in order to achieve high-quality films. The correlation of the linewidth with the surface roughness and the surface Fe deficiency indicates that the linewidth contains a significant contribution from surface defects. This observation was supported by experiments on films with surface treatment and films of different thicknesses, as discussed in the next chapter.

CHAPTER 4

SURFACE DEFECTS-CAUSED DAMPIN IN YIG NANO FILMS

4.1 Surface defects-associated two-magnon scattering

The experimental data presented in Chapter 3 show that the FMR linewidth in YIG nano films increases with both surface roughness and surface Fe deficiency. One can explain this observation in terms of two-magnon scattering: the film surface imperfection serves as sources for the scattering of the uniform FMR mode into non-uniform spin-wave modes, and such film imperfection-caused scattering manifests themselves as an increase in the FMR linewidth.[16,43]

The above explanation gives rise to two expectations as follows. First, if a surface treatment is carried out to reduce surface defects, one can expect weaker two-magnon scattering and a corresponding reduction in FMR linewidth ΔH_{FMR}. Second, an increase in film thickness should decrease the contribution of the film surface-associated damping to the overall damping of the film and thereby lead to a reduction in ΔH_{FMR}. Indeed, both expectations are verified experimentally, as discussed below.

---

[43] R. D. McMichael and P. Krivosik, IEEE Trans. Magn. **40**, 2 (2004).

4.2 Surface treatment by low-energy ion etching

The surface treatment was carried out through low-energy Ar^+ ion etching in a sputtering chamber, with the YIG film attached to the substrate holder and the RF source also applied to the substrate holder. During the etching, the sputtering power was 10 W, the film temperature was 400 °C, and the film was rotated at 40 rpm. Prior to the etching, the sputtering chamber had a base pressure of 3.0×10^{-8} Torr.

Figures 14 and 15 show data that demonstrated the reduction of ΔH_{FMR} via the surface treatment. In Fig. 14, graphs (a)-(c) present 9.5 GHz FMR profiles for an 11-nm-thick film before and after a low-energy ion etching process, as indicated. Graphs (d) and (e) show the FMR linewidth ΔH_{FMR} and FMR field H_{FMR} as a function of etching time t_e. Graph (f) gives the effective saturation induction $4\pi M_{\mathrm{eff}}$ values, which were estimated with

$$\omega = 2\pi|\gamma|\sqrt{H_{\mathrm{FMR}}\left(H_{\mathrm{FMR}} + 4\pi M_{\mathrm{eff}}\right)} \tag{4.1}$$

where ω is the angular frequency used in FMR measurements and $|\gamma|$=2.8 GHz/kOe is the absolute gyromagnetic ratio. The calculations used the H_{FMR} values given in graph (e). Since the in-plane anisotropy field in YIG nano films is relatively weak as shown in Fig. 13(d), it was not considered in the calculations. Figure 15 gives surface AFM images and XPS spectra of the 11-nm-thick film before and after the surface etching, as indicated.

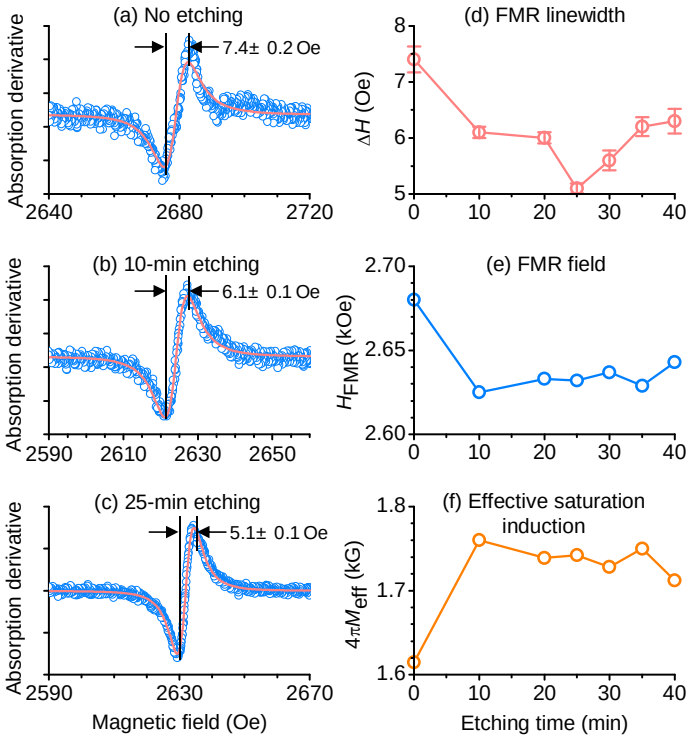

FIG. 14. Graphs (a), (b), and (c) give FMR profiles for an 11-nm-thick YIG film before etching, after 10-minute etching, and after 25-minute etching, respectively. Graphs (d), (e), and (f) show FMR linewidth, FMR field, and effective saturation induction of the YIG film, respectively, as a function of etching time.

It is evident from the data in Figs. 14 and 15 that appropriate ion etching can significantly improve the film surface quality and reduce the FMR linewidth. When $t_e \leq 25$ min, an increase in t_e results in a smoother surface, a lower deficiency in Fe, and a smaller ΔH_{FMR}. When t_e is increased further, however, the film quality becomes worse. The change in the FMR linewidth with t_e is clearly shown in Fig. 14(a)-(d). The change in the surface smoothness is as follows: a 25-min etching led to a significant reduction in the surface roughness, from 0.24±0.01 nm to 0.12±0.01 nm; a 40-min etching did not lead to a further reduction, but to a larger roughness which is 0.17±0.01 nm. The analysis of the XPS data indicates that the surface Fe deficiency changes with t_e in a similar manner: a 25-min etching resulted in a decrease of the Y:Fe ratio

from 3.0:2.6 to 3.0:3.2, and a 40-min etching resulted in a slightly larger Y:Fe ratio which was 3.0:3.0.

Therefore, one can see that (1) the effect of the etching time on the quality of the film surface is consistent with that on the FMR linewidth and (2) there exists an optimal etching time

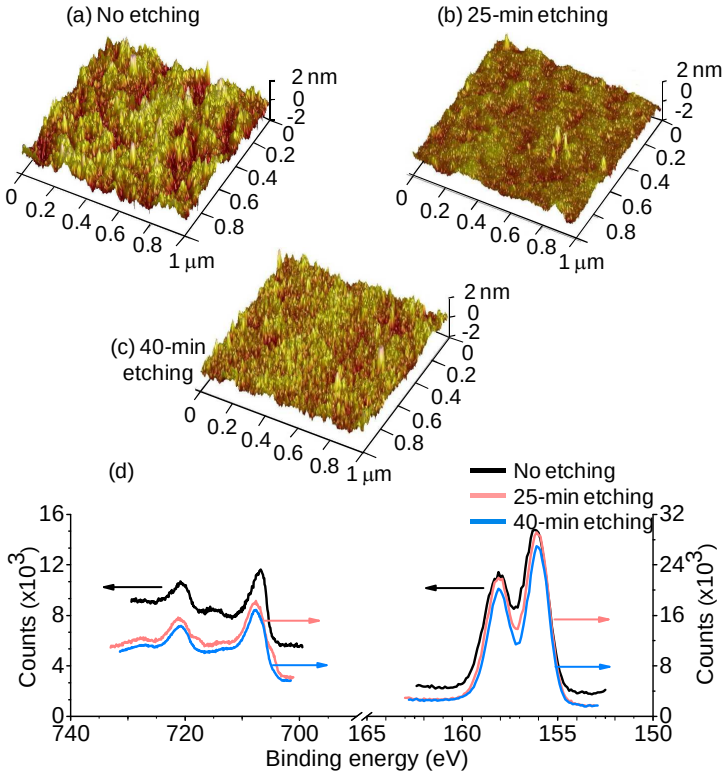

FIG. 15. Surface AFM images and XPS spectra for an 11-nm-thick YIG film before and after surface etching, as indicated.

(t_e=25 min). Future work is of interest that explains the existence of an optimal etching time and optimizes various etching control parameters for the realization of films with even higher quality. Furthermore, the data in Fig. 14(f) indicate that the etching results in an increase in $4\pi M_{\text{eff}}$. This increase might result from the etching-caused smaller Fe deficiency, as indicated

by the XPS data, and possible etching-induced surface anisotropy. The etching process might also give rise to changes in Fe states,[44] which affect both the magnetization and anisotropy field.

4.3 Thickness dependent FMR linewidth

The results from Figs. 14 and 15 undoubtedly verify the first expectation described above. The second expectation is verified by the FMR data obtained for films of different thicknesses. Figure 16 shows the data obtained for a 5.6-nm-thick film, an 11-nm-thick film, and a 19-nm-thick film, which were deposited at the same PLD conditions (T_s =790 °C and f_L =1 Hz). The symbols in graph (a) show H_{FMR} as a function of $\omega/2\pi$. The curves in graph (a) give fits using Eq. (4.1) and the above-cited parameters. The only fitting parameter is $4\pi M_{eff}$, which is 1.67 kG for the 11-nm-thick film and 1.88 kG for the 19-nm-thick film. The differences of these values from the value expected for YIG crystals (1.75 kG)[7] are within 8%. In graph (b), the symbols show ΔH_{FMR} values measured at different frequencies, and the lines present the fits with $\Delta H_{FMR} = \Delta H_0 + \frac{1}{\sqrt{3}} \frac{2\alpha_{eff}}{|\gamma|} \frac{\omega}{2\pi}$, where ΔH_0 describes film inhomogeneity-caused line broadening and α_{eff} is the effective damping constant. The linear fitting yields α_{eff} =(3.2±0.3)×10^{-4} for the 11-nm-thick film and α_{eff} =(2.3±0.1)×10^{-4} for the 19-nm-thick film. These data clearly indicate that the thicker the film is, the smaller both the FMR linewidth and the effective damping constant are. It should be mentioned that the two-magnon scattering-produced linewidth generally changes with frequency in a nonlinear manner. This

[44] C. Burrowes, B. Heinrich, B. Kardasz, E. A. Montoya, E. Girt, Y. Sun, Y.-Y. Song, and M. Wu, Appl. Phys. Lett. **100**, 092403 (2012).

nonlinear response, however, can be quasi-linear at low frequencies for certain sample configurations.[45]

Two notes should be made. First, although the XPS analysis yields no information on the Fe deficiency situation in the film volume, it is very likely that the Fe deficiency in the film volume is much smaller than that on the film surface. This is because the $4\pi M_{\text{eff}}$ values cited above are all close to the standard saturation induction of bulk YIG crystals, and the XRD spectra confirmed the crystalline YIG phase. Second, considering the almost perfect matching between the YIG and GGG lattice constants, one can expect that the defects at the YIG/GGG interface are fewer than those at the YIG surface and thereby make less contributions to the overall linewidth than the surface defects. Future work that verifies this expectation is of great interest.

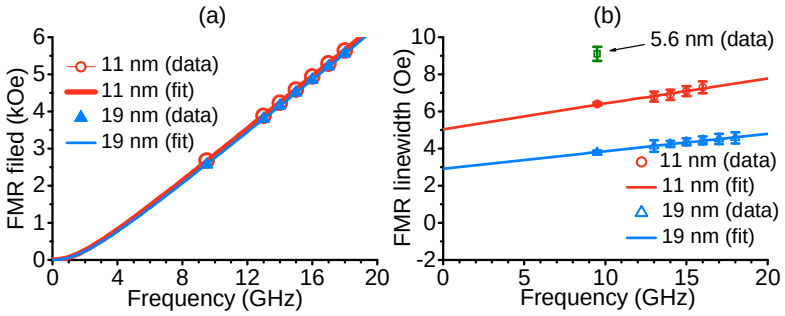

FIG. 16. FMR data (symbols) and theoretical fits (curves and lines) for YIG films of different thicknesses. Graph (a) shows the FMR field as a function of frequency. Graph (b) shows the FMR linewidth obtained at different frequencies.

[45] K. Lenz, H. Wende, W. Huch, K. Baberschke, K. Nagy, and A. Jánossy, Phys. Rev. B **73**, 144424 (2006).

4.4 Summary

In summary, the above-presented results confirm that the surface imperfection makes notable contributions to the FMR linewidth and damping of YIG nano films. Although the damping constants cited above are one to two orders of magnitude smaller than that in metallic nano films, it is expected that one can further reduce the damping of YIG nano films through the use of higher T_s and lower f_L as well as the optimization of the surface etching process.

CHAPTER 5

SPIN PUMPING AT NANO YIG/NORMAL METAL INTERFACES

Effectiveness of spin angular momentum transfer across YIG/NM interfaces is probably the most fundamental issue to be addressed in the emerging research field of YIG-based spintronics. One typically uses the spin mixing conductance $g_{\uparrow\downarrow}$ to describe the interfacial momentum transfer efficiency, and the value of $g_{\uparrow\downarrow}$ depends critically on the spin transmission and reflection coefficients at the interface. The spin mixing conductance has been determined experimentally for many ferromagnetic metal (FM)/NM interfaces; and the experimental values have often agreed with theoretical predictions.[46,47,48] The spin mixing conductance at the YIG/NM interfaces may significantly differ from that at the FM/NM interfaces due to the insulating feature of the YIG layer. The phase of the reflection parameter also becomes a key factor. The transfer of spin angular momentum at YIG/NM interfaces is realized through s-d

[46] Y. Tserkovnyak, A. Brataas, and G. E. W. Bauer, Phys. Rev. Lett. **88**, 117601 (2002).
[47] B. Heinrich, Y. Tserkovnyak, G. Woltersdorf, A. Brataas, R. Urban, and G. E.W. Bauer, Phys. Rev. Lett. **90**, 187601 (2003).
[48] B. Kardasz, O. Mosendz, B. Heinrich, Z. Liu, and M. Freeman, J. Appl. Phys **103**, 07C509 (2008).

exchange interactions, where “s” refers to the conduction electrons in the NM layer and “d” refers to the local electrons in the YIG layer.[49]

5.1 **About spin pumping**

In a ferromagnetic thin film with an adjacent normal metal (NM) layer, the precession of the magnetization produces a spin current that flows from the ferromagnet/NM interface into the NM layer. This effect is known as spin pumping. Considerable work has been carried out on spin pumping in ferromagnetic metal (FM)/NM structures since the early 2000s.[23,46,47,50,51] Very recently, spin pumping has also been observed in ferromagnetic insulator (FI)/NM systems.1’[44,52,53,54,55,56,57]

Spin pumping involves the transfer of spin angular momentum at the ferromagnet/NM interface. This spin transfer manifests itself as two main effects, a pure spin current in the NM film and a damping torque for the magnetization precession in the ferromagnetic film. Theoretical study indicates the real part of spin mixing conductance plays the dominant role in the angular momentum transfer at the FM/NM interface. $\mathrm{Re}\left(g_{\uparrow\downarrow}\right)$ is defined by the equation[46,54]

[49] S. Takahashi, E. Saitoh, and S. Maekawa, J. Phys. Conf. Ser. **200**, 062030 (2009).
[50] R. Urban, G. Woltersdorf, and B. Heinrich, Phys. Rev. Lett. **87**, 217204 (2001).
[51] S. Mizukami, Y. Ando, and T. Miyazaki, Phys. Rev. B **66**, 104413 (2002).
[52] C. W. Sandweg, Y. Kajiwara, K. Ando, E. Saitoh, and B. Hillebrands, Appl. Phys. Lett. **97**, 252504 (2010).
[53] C. W. Sandweg, Y. Kajiwara, A. V. Chumak, A. A. Serga, V. I. Vasyuchka, M. B. Jungfleisch, E. Saitoh, and B. Hillebrands, Phys. Rev. Lett. **106**, 216601 (2011).
[54] B. Heinrich, C. Burrowes, E. Montoya, B. Kardasz, E. Girt, Y.-Y. Song, Y. Sun, and M. Wu, Phys. Rev. Lett. **107**, 066604 (2011).
[55] H. Kurebayashi, O. Dzyapko, V. E. Demidov, D. Fang, A. J. Ferguson, and S. O. Demokritov, Nature Mater. **10**, 660 (2011).
[56] L. H. Vilela-Leão, C. Salvador, A. Azevedo, and S. M. Rezende, Appl. Phys. Lett. **99**, 102505 (2011).
[57] V. Castel, N. Vlietstra, J. Ben Youssef, and B. J. van Wees, Appl. Phys. Lett. **101**, 132414 (2012).

$$g_{\uparrow\downarrow} = \frac{1}{2}\sum_m \left(\left| r_{\uparrow,m} - r_{\downarrow,m} \right|^2 + \left| t_{\uparrow,m} - t_{\downarrow,m} \right|^2 \right) \tag{5.1}$$

where *r* and *t* are the electrons' reflectivity and transmission coefficients at FM/NM interface, respectively. The sum variable, *n*, refers to the number of transport channels, which was learned from the quantum electric transport theory. Simply speaking, if the transport is ballistic type, which means no scattering, there is only one left or right moving state on each energy level. This ideal situation is called single channel model, i.e. *n*=1. Corresponding to the energy band graph, the electrons have only one path to move from left/right chemical energy level to right/left level.

In the real system, the interfacial electrons have multiple transverse modes of moving from the left/right lead to the right/left lead. Each transverse mode defines a transport channel. That means the electrons have *n* (*n*>1) ways to move from one energy level to another in the energy band graph.

However, Eq. (5.1) is only true when the FM layer is conductive. For the insulating FM layer, such as YIG, no electron can transmit into the FM layer, and the transmission coefficient thereby equals zero. On the other hand, the reflectivity coefficient has the amplitude of one and is expressed in the form of $\mathbf{r}_n^{\uparrow\downarrow} = 1 \times e^{i\varphi^{\uparrow\downarrow}}$. Hence, the real part of spin mixing conductance in the insulator FM/NM structure can be simplified to be

$$\mathrm{Re}\left(\mathbf{g}_{\uparrow\downarrow}\right) = \sum_n \left(1 - \cos\left(\varphi_n^{\uparrow} - \varphi_n^{\downarrow}\right)\right) \tag{5.2}$$

From the experimental perspective, it is hard to determine $\mathrm{Re}\left(\mathbf{g}_{\uparrow\downarrow}\right)$ by measuring the phase difference between the spin-up and spin-down electrons. Alternately, one can determine $\mathrm{Re}\left(\mathbf{g}_{\uparrow\downarrow}\right)$ by measuring the spin pumping-produced damping enhancement in the material, as explained below.

The angular momentum transfer involved in the spin pumping process creates a torque which enhances the damping of the magnetization precession in the FM layer. Based on Eq. (2.1), one can derive the expression of spin pumping-associated damping. One can first define the spin pumping-produced spin current $\mathbf{J}_s$ as the rate of the angular momentum transfer per unit area. Then the rate of the angular momentum transfer per unit volume can be written as[46,47]

$$\frac{\mathbf{J}_s}{M_s \cdot 1 \cdot d} = \frac{\hbar}{4\pi M_s} \mathrm{Re}\left(g_{\uparrow\downarrow}\right) \frac{1}{d} \hat{\mathbf{m}} \times \frac{\partial \hat{\mathbf{m}}}{\partial t} \tag{5.3}$$

where d and M_s are the thickness and saturation magnetization of the FM layer, respectively. Multiplying $-|\gamma|$ on both the sides of the angular momentum dynamic equation

$$\frac{\partial \hat{\mathbf{l}}}{\partial t} = \mathbf{m} \times \mathbf{H} - \frac{\hbar}{4\pi M_s} \mathrm{Re}\left(g_{\uparrow\downarrow}\right) \frac{1}{d} \hat{\mathbf{m}} \times \frac{\partial \hat{\mathbf{m}}}{\partial t} \tag{5.4}$$

one obtains

$$\frac{\partial \mathbf{m}}{\partial t} = -|\gamma| \mathbf{m} \times \mathbf{H} + \frac{\hbar|\gamma|}{4\pi M_s} \mathrm{Re}\left(g_{\uparrow\downarrow}\right) \frac{1}{d} \hat{\mathbf{m}} \times \frac{\partial \hat{\mathbf{m}}}{\partial t} \tag{5.5}$$

Comparing it with the torque equation

$$\frac{\partial \mathbf{m}}{\partial t} = -|\gamma| \mathbf{m} \times \mathbf{H} + \alpha_{sp} \hat{\mathbf{m}} \times \frac{\partial \hat{\mathbf{m}}}{\partial t} \tag{5.6}$$

one can write the spin pumping-induced damping as

$$\alpha_{sp} = \frac{\hbar|\gamma|}{4\pi M_s} \mathrm{Re}\left(g_{\uparrow\downarrow}\right) \frac{1}{d} \quad \text{or} \quad \alpha_{sp} = \frac{g\mu_B}{4\pi M_s} \frac{\mathrm{Re}\left(g_{\uparrow\downarrow}\right)}{d} \tag{5.7}$$

where μ_B is the Bohr magnetron and g, $4\pi M_s$, and d are the Landé factor, saturation induction, and thickness of the FM layer, respectively. Equation (5.7) gives the quantitative relationship between the momentum transfer and the spin pumping-induced damping enhancement of the FM

layer. Thus, one can first determine the spin pumping damping through FMR measurements and then use Eq. (5.7) to evaluate the spin mixing conductance.

5.2 Spin pumping at YIG/Au/Fe interfaces

Since spin pumping is an interfacial effect, the damping enhancement can only be observed in the nanometer-thick FM films. The low-damping nano YIG films discussed in previous chapters have been used to study the spin pumping at the magnetic insulator (MI)/NM interface[54].

9-nm-thick YIG films were successfully deposited on single-crystal GGG substrates by PLD techniques with optimized deposition conditions. B. Heinrich *et al*. built the multilayer structures on the top of the YIG films by molecular beam epitaxy techniques. The whole structure is GGG/YIG/Au/Fe/Au. The spin pumping occurs at the YIG/Au interfaces. The Fe layer acts as a spin sink to dissipate spin currents and allow for the continuous generation of spin currents at the YIG/Au interface. To determine the spin mixing conductance at the YIG/Au interface, one only needs to measure the spin pumping-induced damping. In this section, the spin pumping is considered as the only contribution to the additional damping. The spin pumping-induced damping is thereby simply equal to the damping of the whole YIG/Au/Fe/Au structure minus the damping of the bare YIG sample. FMR techniques are used to measure the damping.

The FMR linewidth has the linear response to the microwave frequency and the fitted slope is proportional to the damping as shown in equation (2.4). In Fig. 17, the solid circles show the FMR data of the bare YIG sample, while the solid squares show the data from the YIG/Au/Fe/Au structure. Note that the data in Fig. 17 are for the FMR in the YIG films only; and the FMR in the Fe layer occurs at significantly different frequencies and therefore does not affect the spin pumping at the YIG/Au interface. After knowing the spin pumping-produced damping, the real part of the spin mixing conductance was calculated by using Eq. (5.6) and the following parameters: d=9 nm, g=2.027, μ_B=9.274×10^{-21} erg/G, and $4\pi M_s$=1.31 kG. The calculated spin mixing conductance for the YIG/Au is 1.2×10^{14}/cm^2. This value is about one order of magnitude smaller in comparison with the spin mixing conductance of the metallic FM/NM

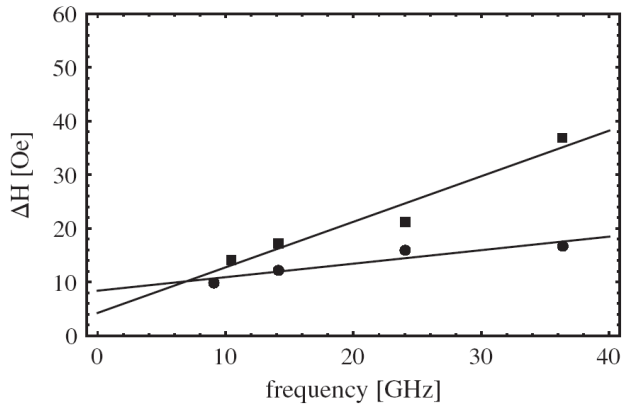

FIG.17. Frequency dependence of FMR linewidth for a bare YIG sample and a YIG/Au/Fe/Au sample.

interface. The much smaller spin mixing conductance in the MI/NM system is due to the zero electron transmission at the interface.

The spin pumping at the YIG/Au interface can be enhanced by the chemical modifications of the YIG film surface through Ar^+ ion beam etching.[44] After low energy and low incidence angle etching at 400 °C, the spin mixing conductance increased by a factor of five in comparison of the untreated YIG/Au interface. Such enhancement is related to the change of the chemical states of Fe and O, which was confirmed by X-ray photoelectronic spectrometry. The data in Table II. indicate that the spin pumping-induced damping increased significantly through Ar^+ etching.

Table II. Ar^+ etching impacts.

Sample	$g_{\uparrow\downarrow}$ $10^{14}cm^{-2}$	$4\pi M_{eff}$ kOe	$\alpha_{untreated}$ 10^{-3}	α_{etched} 10^{-3}	α_s 10^{-3}	α_d 10^{-3}
S1		1.958	0.5			
S2	0.9	1.706			0.7	
S3		1.728	0.5	0.3	1.4	
S4	4.9	2.116	0.5	0.5		6.9
S5	5.0	1.997		0.3		6.9
S6	3.6	2.031	0.3	1.4		6.1

5.3 **Spin pumping at YIG/Cu interfaces**

The last section presents the determination of the spin mixing conductance at an YIG/Au interface. Will one obtain similar values in other YIG/NM interfaces? To answer this question, the spin mixing conductance was determined for YIG/Cu interfaces, as discussed below.

Figure 18 shows the FMR linewidth vs. frequency responses for the bare YIG, YIG/Cu, and YIG/Cu/Pt samples. The symbols refer to the experimental data, while the lines show the

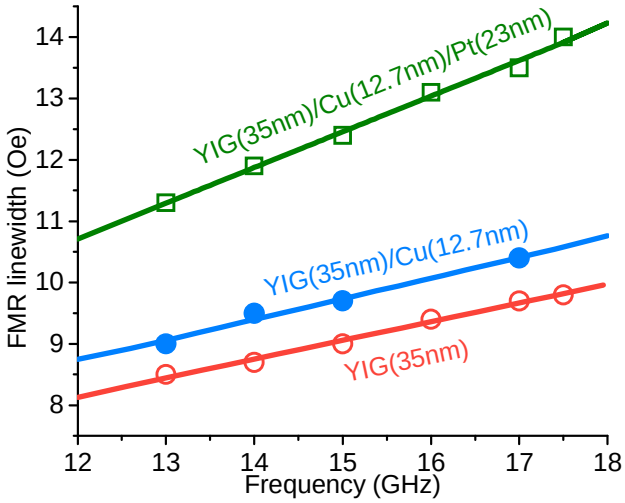

FIG. 18. FMR linewidth as a function of frequency for three samples, as indicated. The symbols show the data, while the lines show fits with Eq. (4.2).

theoretical fits with Eq. (4.2). Table III presents the effective damping constant (α_{eff}) values for eight samples. These values were obtained through the fitting of the linewidth vs. frequency data with Eq. (4.2), as shown representatively in Fig. 18. The error bars give the corresponding standard errors in the fitting. The thicknesses of the samples were given in Fig. 18 as well as Table III. For all the samples, the YIG and Pt thicknesses are 35 nm and 23 nm, respectively. All the samples were prepared by PLD techniques. The details about the PLD techniques were demonstrated in Chapter 3. The main PLD control parameters for the growth of the YIG, Cu, and Pt layers are summarized in Table IV.

Table III. Effective damping constants (α_{eff}) of YIG, YIG/Cu, and YIG/Cu/Pt samples.

Sample	**Damping constant α_{eff}**
YIG(35nm)	$(8.7\pm0.4)\times10^{-4}$
YIG(35nm)/Cu(1.4nm)	$(11.5\pm0.8)\times10^{-4}$
YIG(35nm)/Cu(2.8 nm)	$(9.5\pm1.0)\times10^{-4}$
YIG(35nm)/Cu(5.5 nm)	$(10.1\pm0.4)\times10^{-4}$
YIG(35nm)/Cu(12.7nm)	$(9.4\pm0.8)\times10^{-4}$
YIG(35nm)/Cu(9.9nm)/Pt(23nm)	$(15.7\pm1.1)\times10^{-4}$
YIG(35nm)/Cu(12.7nm)/Pt(23nm)	$(16.3\pm0.6)\times10^{-4}$
YIG(35nm)/Cu(16.8nm)/Pt(23nm)	$(16.8\pm1.7)\times10^{-4}$

The data in Fig. 18 and Table III together show two significant results. First, the growth of a Cu layer onto the YIG film yields small increases in the FMR linewidth and damping constant of the YIG film. These increases might indicate that the Cu growth process slightly enhanced the imperfection on the YIG surface. As discussed in Chapter 4, the surface imperfection can serves as the sources of two-magnon scattering and thereby contributes to the damping increase of the YIG nano films. There also exists another contribution: the spin pumping at the YIG/Cu interface, but this contribution should be very small due to the fact that the thicknesses of the Cu films in the YIG/Cu samples are all significantly smaller than the spin diffusion length in Cu ($\lambda_d \approx 500$ nm).[58]

[58] T. Kimura, J. Hamrle, and Y. Otani, Phys. Rev. B **72**, 014461 (2005).

Table IV. Main control parameters for pulsed laser deposition (PLD)

PLD parameters	YIG	Cu	Pt
Laser pulse energy fluence (J/cm^2)	1.7	1.3	1.3
Laser pulse duration (ns)	30	30	30
Laser pulse repetition rate (Hz)	2	5	5
Substrate-to-target distance (cm)	7.0	5.0	5.0
Substrate temperature (ºC)	790	25	25
Base pressure ($\times 10^{-7}$ Torr)	3.4	7.3	6.7

Second, the growth of a Pt capping layer onto a YIG/Cu sample results in rather significant increases in both the FMR linewidth and damping constant. For example, the growth of a 23-nm-thick Pt layer onto the YIG(35 nm)/Cu(12.7 nm) sample gave rise to an increase in the damping constant of about 73%. This damping enhancement is due to the fact that the Pt layer had a thickness larger than the spin diffusion length in Pt ($\lambda_d \approx 1.4$ nm[59] or 10 nm[60]) and hence effectively dissipated the spin current from the YIG/Cu interface. The spin mixing conductance at YIG/Cu interface was evaluated through the measurement of the additional damping caused by spin pumping.

Table V gives the spin pumping-induced damping α_{sp} and the calculated $\mathrm{Re}(g_{\uparrow\downarrow})$ values for three YIG/Cu/Pt samples. α_{sp} was estimated by the damping values in Table III and the spin mixing conductance $\mathrm{Re}(g_{\uparrow\downarrow})$ was calculated by using Eq. (2.2) with $4\pi M_s$=1.3 kG and g=2.02.[54]

[59] L. Liu, R. A. Buhrman, and D. C. Ralph, arXiv:111.3702 (2012).
[60] L. Vila, T. Kimura, and Y. Otani, Phys. Rev. Lett. **99**, 226604 (2007).

All the three samples have the similar spin mixing conductance values and the average is very close to that at the YIG/Au interface. This result suggests that the efficiency of spin angular momentum transfer at the YIG/NM interface is independent of the NM material selection.

Table V. Damping due to spin pumping and spin mixing conductance in YIG/Cu/Pt samples.

Sample	α_{sp}	**Re($g_{\uparrow\downarrow}$)**
YIG(35nm)/Cu(9.9nm)/Pt(23nm)	5.6×10^{-4}	1.4×10^{14} cm^{-2}
YIG(35nm)/Cu(12.7nm)/Pt(23nm)	6.2×10^{-4}	1.5×10^{14} cm^{-2}
YIG(35nm)/Cu(16.8nm)/Pt(23nm)	6.7×10^{-4}	1.6×10^{14} cm^{-2}

In this experiment, all the NM layers were directly grown on the as-deposited YIG films without any surface pre-treatment. Since the low-energy ion etching should be helpful to reduce both the surface Fe deficiency and surface roughness of YIG nano films, future work is of great interest that optimizes the ion etching process to further improve the efficiency of spin angular momentum transfer at YIG/NM interfaces.

5.4 **Summary**

In this chapter, we studied the spin pumping effect at YIG/NM interfaces. The important physics parameter – the spin mixing conductance was determined via the FMR measurements. The value of the spin mixing conductance at the YIG/NM interfaces is about 1/10 of that at Fe/NM interfaces. To enhance the efficiency of angular momentum transfer at the interface, one can use the low energy and low incident angle Ar^+ ion beam to etch the YIG film surface. This etching can change the chemical states of Fe and O and thereby lead to the enhancement of the spin pumping effect at the YIG/NM interface.

CHAPTER 6

DAMPING ENHANCEMENT IN YIG NANO FILMS DUE TO PLATINUM CAPPING LAYERS

6.1 Damping in YIG/Pt bilayer structures

Generally speaking, damping in a magnetic material can be realized through two main routes.[16,17,43] One route is the redistribution of energy within the magnetic subsystem through magnon-magnon scattering, such as three- and four-magnon scattering and the scattering of magnons upon material imperfections as discussed in Chapter 4. The other is the transfer of energy from the magnetic subsystem to non-magnetic subsystems, such as phonons and electrons. In a ferromagnetic thin film with an adjacent normal metal (NM) film, there exists another damping route - spin pumping, as discussed in Chapter 5. The damping due to spin pumping is fundamentally different from the two main routes mentioned above: (1) it engages energy transfer to external systems, not to the subsystems within the same material; and (2) it is an interface effect and hence plays an important role only for thin films.[23,46,51] This chapter presents experimental evidence for the presence of a new damping in ferromagnetic thin films. The samples consist of YIG nano films capped by Pt films. It is found that, when it is 3 nm or thicker, the Pt capping layer gives rise to an extra damping that is not only significantly larger

than the expected damping from spin pumping (α_{sp}), but is also accompanied by a shift in the ferromagnetic resonance (FMR) field. It is also found that this new damping can be switched off by the addition of a thin Cu spacer in-between the YIG and Pt films. The new damping originates from the ferromagnetic ordering in the Pt atomic layers near the YIG/Pt interface and the dynamic exchange coupling between the "ordered" Pt spins and the spins in the YIG film. The FM ordering of the Pt electrons is due to the proximity effect (MPE) at the YIG/Pt interface.[61,62,63,64,65,66] The dynamic YIG-Pt coupling allows for the transfer of a part of the intrinsic damping in the ordered Pt to the YIG film. Due to the FM ordering of the Pt atomic layers at the interface, conventional spin pumping from the YIG film to the Pt film does not occur. However, there exists spin pumping from the FM Pt into the paramagnetic (PM) Pt, which contributes to the damping of the FM Pt. The use of a Cu spacer switches off the MPE and thereby turns off the new damping. The damping is denoted as α_{MPE} below, as its origin is associated with the MPE.

Three important points should be emphasized. (1) Although the results presented below were obtained with YIG/Pt structures, one can expect similar results in any ferromagnet/NM systems where the proximity effect exists, including Ni/Pt,[62] NiFe/Pt,[64] Fe/Pd,[61] and NiFe/Pd.[63]

---

[61] E. E. Fullerton, D. StoefBer, K. Ounadjela, B. Heinrich, Z. Celinski, and J. A. C. Bland, Phys. Rev. B **51**, 6364 (1995).

[62] F. Wilhelm, P. Poulopoulos, G. Ceballos, H. Wende, K. Baberschke, P. Srivastava, D. Benea, H. Ebert, M. Angelakeris, N. K. Flevaris, D. Niarchos, A. Rogalev, and N. B. Brookes, Phys. Rev. Lett. **85**, 413 (2000).

[63] W. E. Bailey, A. Ghosh, S. Auffret, E. Gautier, U. Ebels, F. Wilhelm, and A. Rogalev, Phys. Rev. B **86**, 144403 (2012).

[64] W. L. Lim, N. Ebrahim-Zadeh, H. G. E. Hentschel, and S. Urazhdin, arXiv:1209.1802 (2012).

[65] S. Y. Huang, X. Fan, D. Qu, Y. P. Chen, W. G. Wang, J. Wu, T. Y. Chen, J. Q. Xiao, and C. L. Chien, Phys. Rev. Lett. **109**, 107204 (2012).

[66] S. Geprägs, S. Meyer, S. Altmannshofer, M. Opel, F. Wilhelm, A. Rogalev, R. Gross, and S. T. B. Goennenwein, Appl. Phys. Lett. **101**, 262407 (2012).

Thus, this work reveals another channel for magnetic damping via energy transfer into external systems. (2) The new damping cannot be described by existing models[51,67] and, therefore, begs for new theoretical studies on damping in ferromagnet/NM systems. (3) Very recently a new research field has appeared that makes use of YIG/Pt heterostructures to study new spin-related physics.[1,2,44,52-57,65,67,68,69,70,71,72,73,74,75] Understanding and control of damping in YIG/Pt structures presented below provide significant implications for the future development of this new field.

6.2 **Samples fabrication and characterization**

The YIG, YIG/Pt, YIG/Cu, YIG/Cu/Pt samples were fabricated by PLD techniques. The main PLD control parameters are given in Table IV. Details on the PLD growth of YIG films are provided in Chapter 3 and also in Ref. [39]. The YIG/Cu and YIG/Cu/Pt samples where the Cu surfaces are naturally oxidized are denoted as YIG/Cu* and YIG/Cu*/Pt, respectively. For these samples, the YIG and Pt layers were grown by PLD techniques, while the Cu layers were deposited by DC sputtering at room temperature. As for the samples discussed in Chapter 3, the crystalline structure of each layer was confirmed by x-ray diffraction measurements, the

[67] S. M. Rezende, R. Rodríguez-Suárez, M. M. Soares, L. H. Vilela-Leão, and A. Azevedo, Appl. Phys. Lett. **102**, 012402 (2013).
[68] M. B. Jungfleisch, A. V. Chumak, V. I. Vasyuchka, A. A. Serga, B. Obry, H. Schultheiss, P. A. Beck, A. D. Karenowska, E. Saitoh, and B. Hillebrands, Appl. Phys. Lett. **99**, 182512 (2011).
[69] E. Padrón-Hernández, A. Azevedo, and S. M. Rezende, Phys. Rev. Lett. **107**, 197203 (2011).
[70] E. Padrón-Hernández, A. Azevedo, and S. M. Rezende, Appl. Phys. Lett. **99**, 192511 (2011).
[71] A. V. Chumak, A. A. Serga, M. B. Jungfleisch, R. Neb, D. A. Bozhko, V. S. Tiberkevich, and B. Hillebrands, Appl. Phys. Lett. **100**, 082405 (2012).
[72] D. Qu, S. Y. Huang, J. Hu, R. Wu, and C. L. Chien, Phys. Rev. Lett. **110**, 067206 (2013).
[73] G. L. da Silva, L. H. Vilela-Leão, S. M. Rezende, and A. Azevedo, Appl. Phys. Lett. **102**, 012401 (2013).
[74] M. B. Jungfleisch, T. An, K. Ando, Y. Kajiwara, K. Uchida, V. I. Vasyuchka, A. V. Chumak, A. A. Serga, E. Saitoh, and B. Hillebrands, Appl. Phys. Lett. **102**, 062417 (2013).
[75] N. Vlietstra, J. Shan, V. Castel, B. J. van Wees, and J. B. Youssef, arXiv:1301.3266 (2013).

thickness of each layer was determined based on the deposition rate and time, the surface roughness was determined by atomic force microscopy measurements, and the ferromagnetic resonance (FMR) was measured in microwave shorted waveguides and cavities with in-plane magnetic fields unless otherwise specified. As in previous chapters, the FMR linewidths presented below all refer to the peak-to-peak linewidths of the FMR power absorption derivative profiles.

6.3 Magnetic proximity induced damping in YIG/Pt

Figure 19 shows the FMR data obtained for ten YIG/Pt samples, for which the YIG film thickness d_{YIG} is 25 nm while the Pt thickness d_{Pt} varies in the 0-20 nm range.

Graphs (a) and (b) give the FMR profiles for a bare YIG sample and a YIG/Pt(20nm) sample, respectively. The circles show the experimental data, while the dashed and solid curves show Lorentzian and Gaussian fits, respectively. Graph (c) gives the Pt capping layer-caused shift of the FMR field H_{FMR} as a function of d_{Pt}. The data in graphs (a)-(c) were obtained with a 9.5 GHz cavity. The inset in graph (b) shows an FMR profile and the ΔH_{FMR} value measured with a shorted waveguide for the sample cited for the data in (b). These data indicate the consistency of the FMR measurements with a shorted waveguide to those with a cavity. Additional measurements indicate that the difference in ΔH for two approaches is usually less than 10%.

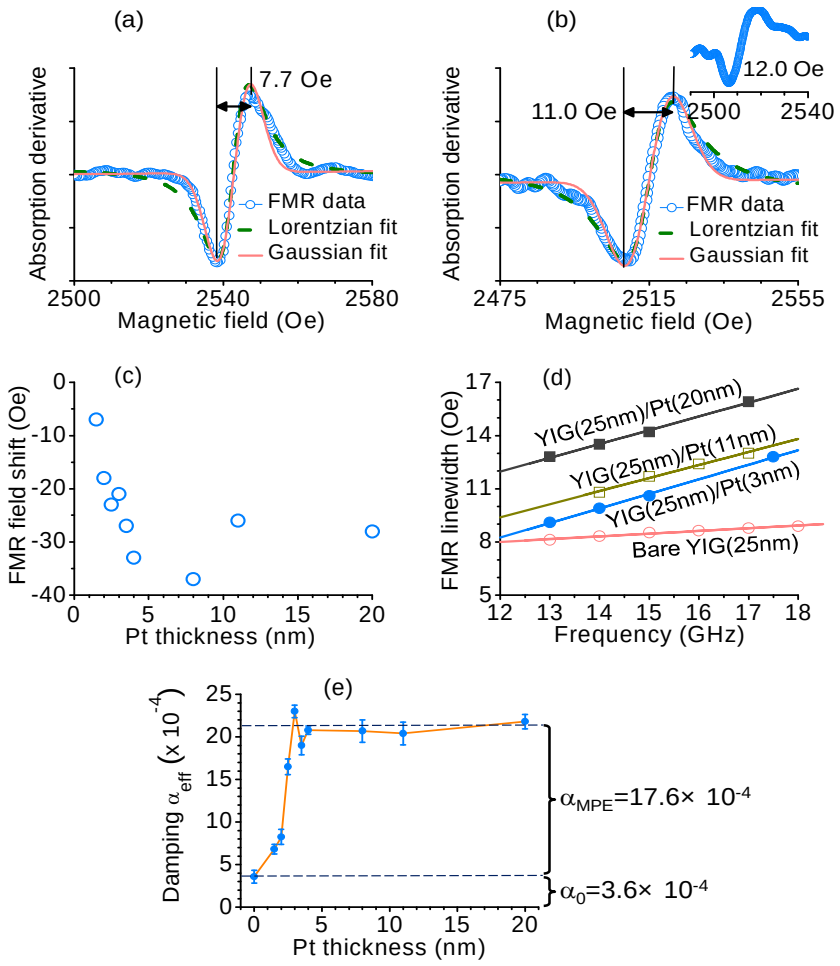

FIG. 19. (a) FMR profile for a bare YIG(25nm) sample. (b) FMR profile for a YIG(25nm)/Pt(20nm) sample. (c) Pt capping layer-caused H_{FMR} change as a function of the Pt thickness. The data in graphs (a)-(c) were obtained at 9.5 GHz. (d) FMR linewidth vs. frequency responses for four samples. (e) Effective damping constant α_{eff} as a function of the Pt thickness.

Graph (d) shows the FMR linewidth ΔH_{FMR} as a function of microwave frequency $\omega/2\pi$ for four samples. The symbols show the experimental data, while the solid lines show theoretical fits with Eq. (4.2). Graph (e) gives the effective damping constant α_{eff} as a function of d_{Pt}. The α_{eff} values were obtained from the fitting of the linewidth vs. frequency responses with Eq. (4.2), as shown representatively in graph (d). The error bars give the standard errors in the fitting. In graph (e), the two components of α_{eff} are also indicated. The component α_0

was the damping constant measured for the bare YIG sample, while α_{MPE} was determined as $\alpha_{\mathrm{MPE}} = \alpha_{\mathrm{eff}} - \alpha_0$

The following results are evident from the data in graphs (a)-(d). (1) The growth of a Pt capping layer on the YIG film leads to a decrease in H_{FMR}, as shown in graphs (a)-(c). (2) The Pt capping layer also results in an increase in ΔH_{FMR}, as shown in graphs (a), (b), and (d). (3) For the fittings in graphs (a) and (b), the Gaussian functions fit slightly better than the Lorentzian functions. In graph (c), all the fittings yield nonzero ΔH_0 values. These two facts indicate that the FMR linewidths contain a non-trivial contribution from film inhomogeneity-caused line broadening.

Graph (e) shows three important results. First, the growth of the Pt capping layer leads to a substantial increase in damping. This damping enhancement is consistent with the above-mentioned increase in FMR linewidth. Second, the α_{eff} vs. d_{Pt} response shows a saturation. When d_{Pt}<3 nm, the damping α_{eff} increases significantly with d_{Pt}; When d_{Pt}>3 nm, α_{eff} is relatively constant. This d_{Pt} dependence is similar to that of the H_{FMR} shift shown in graph (c). Third, the new damping α_{MPE} is substantially larger than spin-pumping damping expected for YIG/NM structures, which is α_{sp}=6.9×10^{-4}. This damping was calculated by the Eq. (2.2) $\alpha_{sp} = \frac{g\mu_B}{4\pi M_s}\frac{\mathrm{Re}\left(g_{\uparrow\downarrow}\right)}{d}$. Note that the Pt thickness at which both the α_{eff} and H_{FMR} shift saturate is close to the length scale reported previously for the dependence of $\mathrm{Re}\left(g_{\uparrow\downarrow}\right)$ on d_{Pt} for bi-layered Permalloy/Pt structures.[76]

[76] Z. Feng, J. Hu, L. Sun, B. You, D. Wu, J. Du, W. Zhang, A. Hu, Y. Yang, D. M. Tang, B. S. Zhang, and H. F. Ding, Phys. Rev. B **85**, 214423 (2012).

The above-presented results derive from the magnetic ordering of electrons in several atomic layers of the Pt film in the close proximity of the YIG film[61-66] and the interfacial exchange coupling between the ordered Pt electrons and the localized electrons in the YIG film. There exist both static and dynamic exchange couplings. The static exchange coupling results in a torque on the magnetization (**M**) in the YIG film that is proportional to **M** and manifests itself as a shift in H_{FMR} shown in graph (c). The dynamic exchange coupling also results in a torque, but this torque is proportional to $\partial\mathbf{M}/\partial t$ and plays a role of an additional damping for the precession of **M**.[77] Via this torque, the Pt film shares its intrinsic damping with the YIG film, resulting in α_{MPE}. This interpretation is supported by the fact that both the "H_{FMR} shift vs. d_{Pt}" and "α_{eff} vs. d_{Pt}" responses show saturation behavior at $d_{Pt}\approx 3$ nm, as shown in graphs (c) and (e). In more detail, as the Pt thickness increases and the Pt film evolves from clusters to a continuous epitaxial film, the interfacial exchange coupling becomes stronger and both the H_{FMR} shift and α_{eff} increase. When $d_{Pt}>3$ nm, however, the growth of additional Pt leads to no further enhancement in the interfacial coupling and the increases of both the H_{FMR} shift and α_{eff} saturate. Note that, since the Pt atomic layers near the YIG/Pt interface are ordered due to the MPE, conventional spin pumping does not take place at the interface and one has $\alpha_{sp}=0$ and $\alpha_{eff}=\alpha_0+\alpha_{MPE}$ as mentioned above.

6.4 Suppression of the new damping by a Cu spacer

To further test the above interpretation, the effects of adding a thin Cu spacer in-between the YIG and Pt films were studied. Cu was chosen because it has a very weak spin-orbit interaction

[77] B. Heinrich and J. F. Cochran, Advances in Phys. **42**, 523 (1993).

and a very long spin diffusion length ($\lambda_d \approx 500$ nm).[58] With an increase in the Cu thickness (d_{Cu}), one can expect a weaker MPE and corresponding decreases in both the H_{FMR} shift and α_{MPE}. At the same time, one can expect spin pumping at the YIG/Cu interface and the presence of α_{sp}. If $d_{Cu} << \lambda_d$, the spin current undergoes very weak dissipation in the Cu spacer but diffuses into and dissipates in the Pt film. For this reason, one can expect a very weak dependence of α_{sp} on d_{Cu} as long as $d_{Cu} << \lambda_d$. For YIG/Cu*/Pt samples, however, one can expect that the presence of the insulating Cu oxide not only eliminates both α_{MPE} and H_{FMR} shift, but also prohibits the presence of α_{sp}.

Figure 20 presents data for seven YIG(35nm)/Cu/Pt(23nm) samples and five YIG(35nm)/Cu samples, for which the thicknesses of both the YIG and Pt films are constant and the Cu

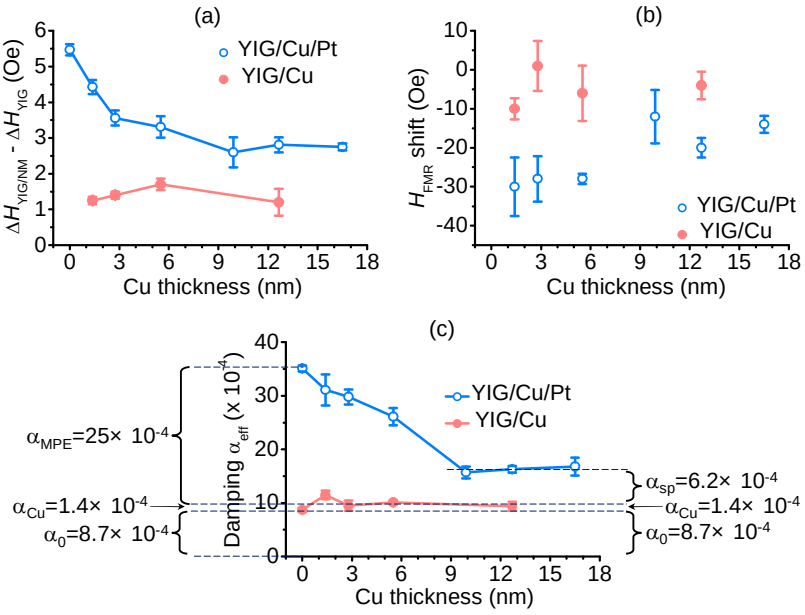

FIG. 20. Data obtained for YIG(35nm)/Cu/Pt(23nm) samples (empty circles) and YIG(35nm)/Cu samples (solid circles). (a) NM layer-caused FMR linewidth change as a function of Cu thickness. (b) NM layer-caused FMR field change as a function of Cu thickness. (c) Effective damping constant as a function of Cu thickness.

thickness d_{Cu} varies in the 0-17 nm range. Graphs (a) and (b) give 9.5 GHz FMR data. Graph (a) gives the NM layer-caused change in the FMR linewidth as a function of d_{Cu}, while graph (b) gives the shift in the FMR field as a function of d_{Cu}. Graph (c) presents the effective damping constant α_{eff} as a function of d_{Cu}. The graph also indicates the components of α_{eff}. In graphs (a) and (b), each point shows the averaged value over 5-10 FMR measurements, and the error bar for each point shows the corresponding standard deviation. In graph (c), the effective damping constants were obtained through the fitting of the FMR linewidth vs. frequency data with Eq. (4.2). Note that the YIG/Cu samples cited here are the same as those cited in Chapter 5.

The data for the YIG/Cu samples indicate that the growth of a Cu layer yields an extra damping (α_{Cu}) which is much smaller than α_0. This agrees with the expectation that the growth of a NM capping layer should not change the relaxation in the YIG film in the absence of the MPE and spin pumping. The spin pumping is absent in these samples because d_{Cu} is much smaller than λ_d. This is supported by the fact that the YIG/Cu samples show very similar α_{eff} values in spite of a relatively wide d_{Cu} range (0-12.7 nm). In the case that spin pumping at the YIG/Cu interface makes significant contributions to α_{eff}, one would expect that α_{eff} increases with d_{Cu}. Although α_{Cu} is small, its presence might indicate that the process of the Cu growth slightly enhances the imperfection on the YIG surface, which gives rise to a damping enhancement in the YIG film.

The data for the YIG/Cu/Pt samples indicate that the addition of a Cu spacer can reduce the H_{FMR} shift, ΔH, and α_{eff} of the YIG/Pt sample. Moreover, the thicker the Cu spacer is, the larger the reductions are. One also can see that for the samples with $d_{Cu} \geq 10$ nm, an additional increase in d_{Cu} does not result in a further reduction in α_{eff}, as shown in graph (c). This

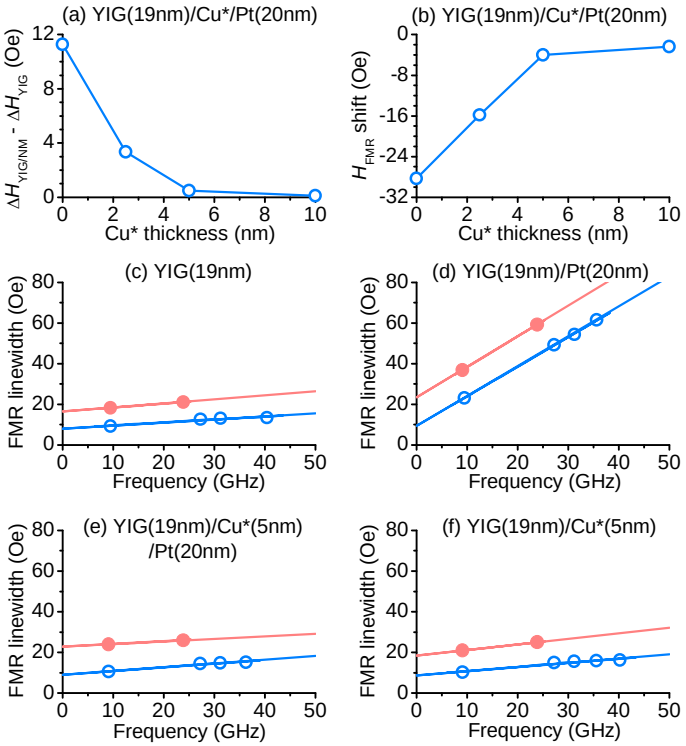

FIG. 21. Data obtained for YIG(19nm)/Cu*/Pt(20nm) samples as well as several control samples. (a) NM layer-caused FMR linewidth change as a function of the Cu thickness. (b) NM layer-caused FMR field shift as a function of the Cu thickness. (c)-(f) FMR linewidth as a function of frequency for four samples. The empty and solid circles show the data from in-plane and out-of-plane FMR measurements, respectively. The lines in (c)-(f) show fits with Eq. (4.2).

indicates that the samples with $d_{Cu}\geq 10$ nm have $\alpha_{MPE}=0$ and $\alpha_{eff}= \alpha_0+\alpha_{Cu}+\alpha_{sp}$. Thus, one can evaluate α_{sp} as $\alpha_{sp}=\alpha_{eff}-\alpha_0-\alpha_{Cu}=6.2\times10^{-4}$ for the YIG/Cu(≥10nm)/Pt samples. Assuming that the growth of a Pt layer on a YIG film also slightly modifies the YIG surface and results in a small damping enhancement as the growth of a Cu layer does, one can then determine α_{MPE} in the YIG(35nm)/Pt(23nm) sample as $\alpha_{MPE}=\alpha_{eff}-\alpha_0-\alpha_{Cu}$, which is also given in graph (c). One can see that α_{MPE} is significantly larger than both α_0 and α_{sp}, similar to the results indicated by the data in Fig. 19(e).

Consider now the YIG/Cu*/Pt samples for which representative data are shown in Fig. 21 and Table VI. In Fig. 21, graphs (a) and (b) present the NM layer-caused changes in FMR linewidth and FMR field, respectively, as a function of the Cu* thickness (d_{Cu*}). The data were measured at 9.5 GHz. Graphs (c)-(f) show the FMR linewidth vs. frequency data for four different samples. In all the graphs, the empty circles show the data from FMR measurements with in-plane magnetic fields, while the solid circles show those obtained from measurements with out-of-plane fields. In graphs (c)-(f), the lines show the fits with Eq. (4.2). The effective damping constants from the fitting are given in Table VI.

Table VI. Effective damping constants for four samples

Sample	**α_{eff} ($\times 10^{-4}$) (in-plane)**	**α_{eff} ($\times 10^{-4}$) (out-of-plane)**
YIG(19nm)	3.58±0.76	4.72
YIG(19nm)/Pt(20nm)	35.36±0.58	36.60
YIG(19nm)/Cu*(5nm)/Pt(20nm)	4.33±0.58	3.41
YIG(19nm)/Cu*(5nm)	4.82±0.62	6.71

Three results are evident from the data in Fig. 21 and Table VI. (1) The Pt capping layer-caused additional damping is substantially larger than both the measured damping for the bare YIG film and the calculated damping for spin pumping. (2) In contrast to the situation for the YIG/Cu/Pt samples, a 5-nm-thick Cu* spacer is sufficient to kill both α_{MPE} and the H_{FMR} shift. This is indicated by the facts that the ΔH_{FMR} values for both the YIG/Cu*(5nm)/Pt and YIG/Cu*(10nm)/Pt samples almost match that of the bare YIG sample, as shown in graph (a),

and the H_{FMR} shifts for both the YIG/Cu*(5nm)/Pt and YIG/Cu*(10nm)/Pt samples are close to zero, as shown in graph (b). (3) There is no evidence of spin pumping in the YIG/Cu*/Pt samples, as indicated by the fact that the α_{eff} values of the YIG/Cu*(5nm) and YIG/Cu*(5nm)/Pt samples are very close to each other and are also close to α_0 (see Table VI). It should be mentioned that although the out-of-plane FMR measurements were carried out at two frequencies only, the α_{eff} values obtained from the linear fitting are all close to those obtained from in-plane FMR measurements. This closeness assures the accuracy of the damping values presented. It also indicates that two-magnon scattering makes small contributions to the damping of the YIG films. It should also be noted that in graphs (c)-(f) the out-of-plane ΔH_{FMR} values are all larger than the corresponding in-plane values. This is mainly because ΔH_0 is larger for out-of-plane FMR measurements than for in-plane measurements. As the YIG films have very weak anisotropy, one can assume the inhomogeneity line broadening is mainly due to the inhomogeneity of the magnetization (ΔM) and one can roughly evaluate the line broadening contribution as $\Delta H_0 = \left(\frac{\partial H_{FMR}}{\partial M}\right)\Delta M$. The coefficient in this equation equals to 1 for out-of-plane measurements but is less than 0.5 for in-plane FMR measurements.

The results from Figs. 20 and 21 together confirm the presence of α_{MPE} in the YIG/Pt structures. Moreover, these results clearly verify the above-discussed expectations: (1) a Cu spacer can decouple the YIG and Pt films and thereby suppresses both the H_{FMR} shift and α_{MPE} and (2) the Cu spacer facilitates the spin pumping of the YIG film in the absence of Cu surface oxidation but does not in the presence of Cu surface oxidation. The results, therefore, support the above interpretation on the origin of α_{MPE}.

In addition, the data in Figs. 20 and 21 also indicate incomplete decoupling between the YIG and Pt films in the YIG/Cu/Pt samples with $0<d_{Cu}<10$ nm and in the YIG/Cu*/Pt samples with $0<d_{Cu*}<5$ nm. The decoupling in these samples is incomplete because the YIG films have relatively large roughness. For a YIG film with a much smoother surface, one can expect

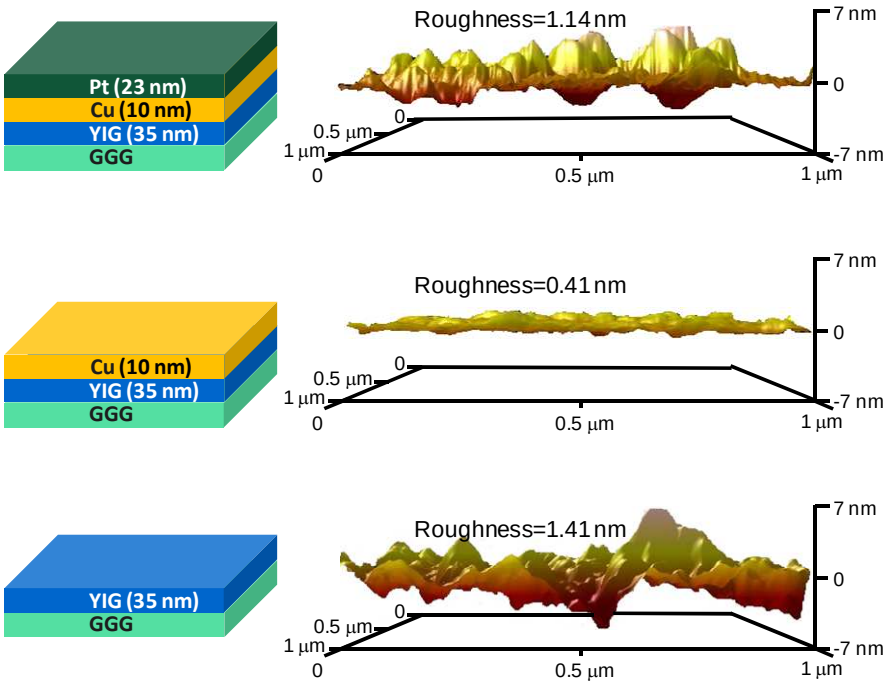

FIG. 22. Atomic force microscopy surface images of three samples.

complete decoupling as well as the complete suppression of α_{new} with a Cu spacer that is much thinner ($d_{Cu}<10$ nm, $d_{Cu*}<5$ nm). Figure 22 gives atomic force microscopy surface images of three samples. The roughness values are averages over the measurements on three different 1μm×1μm areas. One can see from Fig. 22 that the YIG/Cu interface has large roughness, while the Cu/Pt interface is relatively smooth. Because of this, it is conceivable that there are

local regions in the YIG/Cu/Pt sample where the YIG-Pt distance is much smaller than the nominal thickness of the Cu layer (10 nm). It should be mentioned that Mizukami *et al*. observed the decrease of damping in NiFe/Cu/Pt with an increase in d_{Cu} and a saturation in the damping reduction at d_{Cu}=200-300 nm.[51] They explained the results with a model that was based on the spin diffusion in the Cu spacer. This model is not applicable to the configuration in this work due to the fact of $d_{Cu}<<\lambda_d$. Recently, Rezende *et al*. proposed a model to explain the large damping in μm-thick YIG thin films with Pt capping layers.[67] This model yields a new damping that is independent of the thickness of the YIG film and, hence, is inconsistent with the above-discussed interpretation. Furthermore, Kajiwara *et al*. developed a model to explain spin pumping at YIG/Pt interfaces, which, however, did not take into account the MPE. It should also be noted that α_{MPE} is expected to scale with $1/d_{YIG}$. However, this scaling is not shown by the above-presented data, although the YIG(19nm)/Pt sample does show much larger α_{MPE} than the YIG(25nm)/Pt and YIG(35nm)/Pt samples. This is because the actual value of α_{MPE} also depends on the properties of the particular YIG/Pt interface. One can also expect a larger H_{FMR} shift in YIG/Pt structures with much thinner YIG films and insignificant shifts in YIG/Pt structures with much thicker YIG films. The latter was indeed reported recently.[57,67]

Consider finally the spin pumping from the FM Pt to the PM Pt. Recent calculations show that the MPE causes the FM ordering of four Pt atomic layers near the YIG/Pt interface. Since the effective thickness of the FM Pt atomic layers is much smaller than d_{YIG}, one can assume that the contribution from the intrinsic damping of the FM Pt to α_{MPE} is very small and the damping α_{sp} due to spin pumping from the FM Pt to the PM Pt dominates α_{MPE}. Thus, one can evaluate $\mathrm{Re}\left(g_{\uparrow\downarrow}\right)$ at the FM Pt/PM Pt interface by

$$\alpha_{\mathrm{MPE}} \approx \frac{g\mu_{\mathrm{B}}\,\mathrm{Re}\left(g_{\uparrow\downarrow}\right)}{4\pi M_{\mathrm{s}} d_{\mathrm{YIG}} + 4\pi M_{\mathrm{FM\text{-}Pt}} d_{\mathrm{FM\text{-}Pt}}} \tag{6.1}$$

where $4\pi M_{\mathrm{FM\text{-}Pt}}$=90 G and $d_{\mathrm{FM\text{-}Pt}}$=0.96 nm are the saturation induction and effective thickness of the FM Pt atomic layers, respectively. Taking the data in Table V, one obtains $\mathrm{Re}\left(g_{\uparrow\downarrow}\right)$ $\approx 4.2\times10^{14}$ cm^{-2}. This value is larger than that at YIG/Au interfaces or YIG/Cu interfaces (Section IV), indicating efficient pumping from the FM Pt to the PM Pt.

6.5 **Summary**

In summary, this chapter demonstrates the presence of a new damping in YIG/Pt systems. This damping is larger than both the damping of the bare YIG film and the contribution from spin pumping and is accompanied by a shift in H_{FMR}. Both the new damping and the H_{FMR} shift can be effectively suppressed by the use of a Cu spacer between the YIG and Pt films. The results indicate that the new damping originates from the interfacial dynamic exchange coupling between magnetically ordered electrons in the Pt and localized electrons in the YIG. The magnetic ordering in the Pt layer is caused by the magnetic proximity effect.

CHAPTER 7

GROWTH AND FMR OF YIG THIN FILMS ON METALS

7.1 Introduction

As demonstrated in the previous chapter, GGG is the substrate of choice for the growth of high-quality YIG films. However, for certain monolithic device applications one needs to grow YIG films on metals. In coupled-line and stripline-type devices, for example, a ground plane is needed under the active layer.[78,79,80] The growth of YIG films on metals, on the other hand, is very challenging due to various problems associated with the oxidation, diffusion, and breakup of the metallic films or substrates during the deposition of YIG films in oxygen at high temperatures. Such problems prohibit the realization of high-quality YIG films on metals. This chapter reports the growth of high-quality YIG thin films on metallic films. Specifically, the chapter reports the growth of YIG thin films on a sandwich structure that consists of a thick

[78] J. Mazur, M. Solecka, R. Poltorak, and M. Mazur, IEEE Proc.-Microw. Antennas Propag. **151**, 477 (2004).
[79] B. K. Kuanr, D. L. Marvin, T. M. Christensen, R. E. Camley, and Z. Celinski, Appl. Phys. Lett. **87**, 222506 (2005).
[80] B. K. Kuanr, Y. V. Khivintsev, A. Hutchison, R. E. Camley, and Z. J. Celinski, IEEE Trans. Magn. **43**, 2645 (2007).

Cu layer sandwiched between two thin cladding layers. The cladding layers are high entropy alloy nitrides (AlCrTaTiZr)N (HEAN).[81,82] These materials have a high oxidation resistance and good thermal stability and, therefore, can prevent both the oxidation and diffusion of the Cu layer. The HEAN/Cu/HEAN layers were deposited on GGG substrates by sputtering. The YIG films were then grown on the sandwich structure by pulsed laser deposition (PLD). The YIG films had a thickness of several hundreds of nanometers and a surface roughness of several nanometers, consisted of (111)-oriented, 90-nm-diameter grains, and showed peak-to-peak ferromagnetic resonance (FMR) linewidths of about 1.1 Oe at 9.45 GHz and about 2.5 Oe at 17.3 GHz.

Three points should be emphasized. (1) Although the YIG films were grown on metals, their FMR linewidths are only five times larger than the smallest linewidth value for YIG crystals[83] and are one to two orders of magnitude smaller than the linewidths of other magnetic films of similar thicknesses.[84,85] (2) The feasibility of growing YIG films on metals provides significant implications for the future development of new types of YIG-based monolithic devices. (3) A recent work demonstrated the growth of hexagonal ferrite thin films on Pt.[86] With the approach demonstrated here, one can expect the possibility of growing hexagonal ferrite films on Cu. Note that Cu is much less expensive than Pt and has been widely used as device ground planes or electrodes.

---

[81] M.-H. Tsai, C.-W. Wang, C.-H. Lai, J.-W. Yeh, and J.-Y. Gan, Appl. Phys. Lett. **92**, 052109 (2008).
[82] S.-Y. Chang and D.-S. Chen, Appl. Phys. Lett. **94**, 231909 (2009).
[83] G. Winkler, *Vieweg Tracts in Pure and Applied Physics: Magnetic Garnets* (Friedr. Vieweg&Sohn Verlagsgesellschaft mbH, Braunschweig, 1981).
[84] S. Y. An, P. Krivosik, M. A. Kraemer, H. M. Olson, A. V. Nazarov, and C. E. Patton, J. Appl. Phys. **96**, 1572 (2004).
[85] N. M. Salansky, B. P. Khrustalev, A. S. Melnik, L. A. Salanskaya, and Z. I. Sinegubova, Thin Solid Films **4**, 105 (1969).
[86] Y. Nie, I. Harward, K. Balin, A. Beaubien, and Z. Celinski, J. Appl. Phys. **107**, 073903 (2010).

7.2 Sample fabrication and structure characterization

The HEAN/Cu/HEAN layers were deposited on 0.5-mm-thick, (111)-oriented GGG substrates by DC sputtering at room temperature. Prior to the deposition of the Cu layers, the base pressure was 2.8×10^{-8} Torr; during the deposition, the pressure of Ar was 3 mTorr and the sputtering power was 70 W. Prior to the deposition of the HEAN layers, the base pressure was 3.0×10^{-8} Torr. During the deposition of the HEAN layers, the gases in the chamber consisted of 70% Ar and 30% N_2, the pressure was kept constant at 6 mTorr, and the sputtering power was set to 100 W.

The PLD growth of the YIG films used a 1" YIG target and was carried out in high-purity oxygen (99.999%). The target-to-substrate distance was kept constant at 4.0 cm. Prior to the deposition, the system had a base pressure of 1.5×10^{-7} Torr. During the deposition, the substrate temperature was kept constant at 650 °C and the oxygen pressure was 0.1 Torr. Immediately after the deposition, the sample was annealed at 650 °C for 10 minutes. The oxygen pressure was increased gradually from 0.1 Torr to 400 Torr through the post annealing process. The cooling of the system was carried out in a 400 Torr oxygen environment at a rate of 2 °C per minute. The deposition used 248 nm KrF excimer laser pulses with an energy fluence of 1.7 J/cm^2, a pulse duration of 30 ns, and a pulse repetition rate of 12 Hz. These deposition parameters were chosen after a systematic optimization process. These parameters played critical roles in the realization of high-quality YIG films reported below.

The structure and composition properties of the YIG/HEAN/Cu/HEAN samples were analyzed through scanning electron microscopy (SEM), x-ray diffraction (XRD), energy dispersive spectroscopy (EDS), and atomic force microscopy (AFM) measurements. The static

magnetic properties were measured by a superconducting quantum interference device (SQUID) magnetometer. The FMR responses were measured with microwave rectangular cavities by field modulation and lock-in detection techniques. The FMR linewidth values discussed below all refer to peak-to-peak linewidths (ΔH_{pp}).

Figures 23 and 24 show representative data on the structure and phase properties of the YIG samples. In Fig. 23, graphs (a) and (b) show the SEM and EDS cross sections, respectively; and graphs (c) and (d) show the SEM and AFM surface images of the same sample, respectively. The data in Fig. 23 indicate three results. First, the images in (a) and (b) show clear boundaries between all the layers. Second, the thickness of each layer estimated from the SEM image is close to that estimated from the EDS image. Third, the YIG film consists of uniform, nanometer-diameter grains. Although not shown in Fig. 23, the EDS measurements also indicate that (1) the YIG layer has a Y/Fe atomic ratio of 0.605, which perfectly matches the ratio (0.600) expected for bulk YIG crystals, and (2) there exist no CuO in the Cu layer and no Cu in the YIG layer. In addition to the surface image shown in (d), the AFM measurements also indicate that (1) the YIG film has a surface roughness of about 7.0 nm and (2) the grains in the YIG film have an average diameter of about 90 nm.

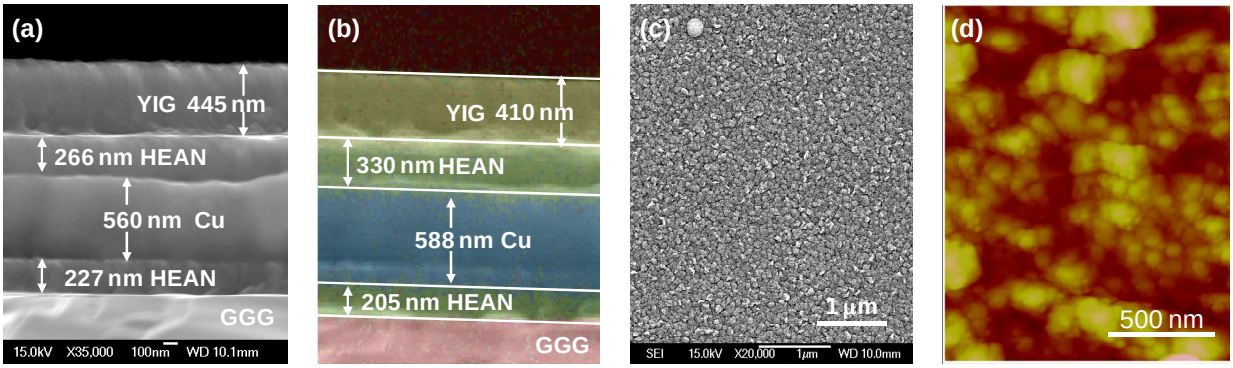

FIG. 23 (same as Fig.7). Structure properties of a YIG/HEAN/Cu/HEAN sample. (a) Cross-section SEM image. (b) Cross-section EDS image. (c) Surface SEM image. (d) Surface AFM image.

Figure 24 presents the XRD data. Graph (a) shows the XRD intensity in a "log10" scale over a wide angle range for the same YIG sample discussed above. Graph (b) shows the (444) peak in (a) in a linear intensity scale and an expanded angle scale. Graph (c) shows the same spectrum in (b), but with both intensity and angle scales expanded. The main peaks shown in (a)-(c) match the peaks expected for the (111)-oriented GGG substrate, as indicated. The appearance of the two (444) peaks results from the coexistence of the $K_{\alpha 1}$ and $K_{\alpha 2}$ components of the X ray. The weak peak in (c) is for the Cu layer, as indicated. These results confirm the (111) orientation of the GGG substrate, indicate the (100) orientation of the Cu layer, and show no notable peaks for other phases, including the YIG film. Graphs (d) and (e) present the XRD rocking curves for the same YIG sample and a bare GGG substrate, respectively. The comparison between the data in (d) and (e) clearly confirms the phase of the YIG film and also indicates the (111) orientation of the YIG film. In addition, the spectra in (a)-(d) show no peaks for the HEAN materials. This is consistent with the amorphous state of the HEAN layers.[81,82]

The results discussed above show that the HEAN layers can effectively prevent the Cu layer from oxidation and diffusion; and this in turn allows for the growth of YIG thin films on the Cu layer. The results show that the YIG film has a uniform thickness, a relatively small surface

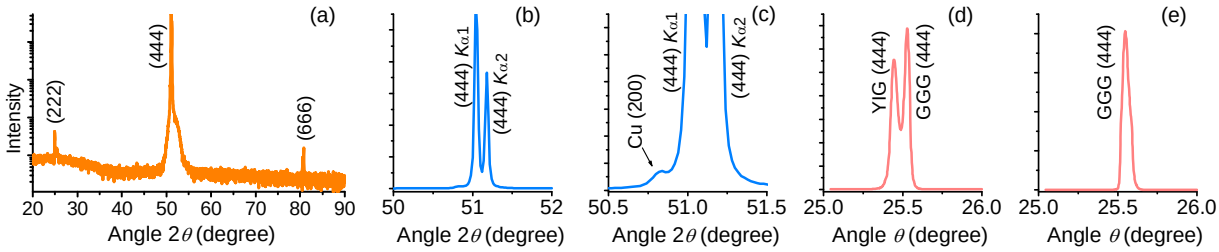

FIG. 24. Graph (a) shows the XRD spectrum of a YIG/HEAN/Cu/HEAN sample. Graph (b) shows the (444) peak in (a) in an expanded angle scale. Graph (c) shows the spectrum in (b) in expanded angle and intensity scales. Graph (d) shows the XRD rocking curve for the (444) $K_{\alpha 1}$ peak in (b). Graph (e) shows the XRD rocking curve for the (444) $K_{\alpha 1}$ peak of a GGG wafer.

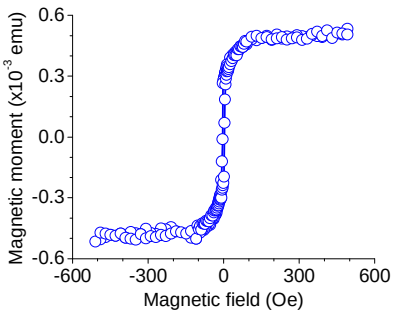

FIG. 25. Magnetic hysteresis loop measured with a magnetic field applied in the film plane.

roughness, an expected Y/Fe ratio, as well as a (111) orientation. These aspects together indicate the high quality of the YIG film and are also accountable for the FMR properties presented below.

7.3 Static magnetic and FMR properties

Figure 25 gives the magnetic moment vs. field hysteresis loop measured with the field applied in the film plane. The data indicate a small coercivity of about 3.8 Oe and a saturation magnetic moment of about 0.5×10^{-3} emu. With this saturation moment and the YIG film thickness estimated from the SEM measurements, the saturation induction $4\pi M_s$ of the film was estimated to be 1.58 kG. With the thickness from the EDS measurements, one obtained a $4\pi M_s$ value of 1.72 kG. Although both the values are smaller than the standard value which is 1.75 kG, the differences are less than 10%. Possible reasons for these differences include the uncertainty in the thickness estimation and the likely existence of a dead layer near the YIG/HEAN interface.

Figure 26 gives representative FMR data for the same YIG sample discussed above. The circles in graphs (a) and (b) show the same FMR power absorption derivative profile measured with a 9.45 GHz cavity. The curve in (a) is a Lorentzian fit, while the curve in (b) is a Gaussian

fit. In graph (c), the circles show the FMR profile measured with a 17.3 GHz cavity, while the curve shows a Lorentzian fit. In graph (d), the circles give the FMR fields at the frequencies cited above, and the solid and dotted curves show the fits with different $4\pi M_s$ values, as indicated. The fitting was carried out with $f_{\mathrm{FMR}} = |\gamma|\sqrt{(H + H_a)(H + H_a + 4\pi M_s)}$, where $|\gamma|$=2.8 MHz/Oe is the absolute gyromagnetic ratio. H_a is an effective anisotropy field and was taken to be 100 Oe for the solid curve and 170 Oe for the dotted curve.

Three important results are evident in Fig. 26. First, the YIG film shows a ΔH_{pp} value of about 1.1 Oe at 9.45 GHz and a value of about 2.5 Oe at 17.3 GHz. These values are only about five times larger than the smallest linewidth for YIG crystals. Second, the Lorentzian fit is much better than the Gaussian fit, as shown in (a) and (b). This indicates that the YIG film is homogeneous. In case that the film is strongly inhomogeneous, the inhomogeneity broadens the FMR linewidth and a Gaussian trial function usually fits the FMR profile better than a

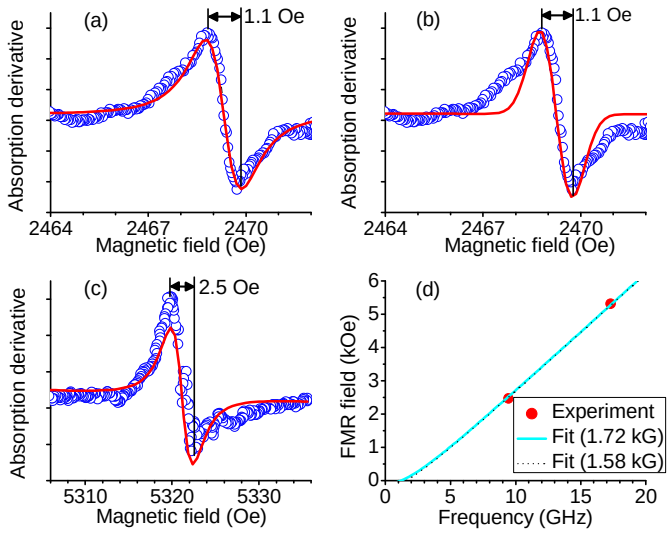

FIG. 26. The circles in (a) and (b) show the same FMR data measured at 9.45 GHz. The circles in (c) show the FMR data measured at 17.3 GHz. The curves in (a) and (c) show Lorentzian fits, while the curve in (b) shows a Gaussian fit. In (d), the circles and curves show the experimental and theoretical FMR fields, respectively.

Lorentzian function.[87] Third, the FMR fields can be fitted well with the standard $|\gamma|$ value and reasonable anisotropy fields.

The results from Fig. 26 clearly indicate that the YIG films have narrow linewidths or low loss. This narrow-linewidth feature is critically associated with the above-described structure properties, including expected atomic ratios, optimal crystalline phase, uniform grains, and small surface roughness. The structure, static magnetic, and FMR properties together prove the high quality of the YIG film. It should be emphasized that this realization of high-quality YIG films on Cu films is attributed to a large extent to the use of the HEAN layers. The HEAN materials have good thermal stability and a high oxidation resistance and thereby serve as barriers to prevent the Cu film from both diffusion and oxidation. In addition, the optimization of the PLD process has also played an important role.

7.4 Summary

High-quality yttrium iron garnet (YIG) thin films were grown on a sandwich structure that consisted of a thick Cu layer and two thin cladding layers. The cladding layers were high entropy alloy nitrides (HEAN) and served as barriers to prevent Cu diffusion and oxidation during the YIG deposition. The Cu and HEAN layers were deposited by sputtering. The YIG films were grown by pulsed laser deposition. The YIG films had a thickness of several hundreds of nanometers, a surface roughness of several nanometers, and (111) orientation. The films showed a peak-to-peak FMR linewidth of 1.1 Oe at 9.45 GHz.

[87] S. S. Kalarickal, P. Krivosik, J. Das, K. S. Kim, and C. E. Patton, Phys. Rev. B **77**, 054427 (2008).

CHAPTER 8

SUMMARY AND OUTLOOK

8.1 Summary and conclusion

The above-presented data and discussions give rise to four important conclusions, as follows:

- It is possible to use PLD techniques to grow high-quality YIG nano films. The 10-nm-thick films show a surface roughness range of 0.1-0.3 nm, an FMR linewidth of about 6 Oe at 10 GHz, and an effective damping constant of about 3.2×10^{-4}. The damping of the YIG nano films includes a notable contribution associated with the surface imperfection, and one can use low-energy ion etching to reduce the surface imperfection and thereby reduce the damping.

- Spin pumping experiments yielded $\mathrm{Re}(g_{\uparrow\downarrow})\approx1.2\times10^{14}$ cm^{-2} for YIG/Au interfaces and $\mathrm{Re}(g_{\uparrow\downarrow})\approx1.6\times10^{14}$ cm^{-2} for YIG/Cu interfaces. The closeness of the two values indicates that the efficiency of spin angular momentum transfer at YIG/NM interfaces is independent of the choice of NM materials. The values are about 10%-15% of those for Fe/NM interfaces, in spite of the fact that YIG films are insulating. Furthermore, these

values can be significantly increased if a treatment is carried out on the YIG surface prior to the deposition of the NM layer.

- The growth of a Pt capping layer onto a YIG nano film can give rise to an increase in the damping of the YIG film. This damping enhancement results from the magnetic ordering of Pt electrons near the YIG/Pt interface and the dynamic exchange coupling between these ordered Pt electrons and the localized electrons in the YIG film. The presence of this new damping may complicate studies involving YIG/Pt structures or limit the device applications of YIG/Pt structures, but it is fortunate that this damping can be completed suppressed by the addition of a thin Cu spacer between the YIG and Pt films.
- It is feasible to grow high-quality YIG thin films on metals. The demonstration used a sandwich structure as the substrate that consisted of a thick Cu layer and two thin cladding layers made of HEAN. The YIG films showed FMR linewidths that were only five times larger than the smallest linewidth for YIG crystals.

8.2 **Future work**

There exists a wide variety of future work that makes use of YIG nano films and is of great fundamental and practical interest. For example, it is of practical significance to develop YIG nano film-based spin torque nano-oscillators that require much lower threshold currents and show much narrower spectral linewidths than transitional metal nano film-based spin torque nano-oscillators. In the context of the topics presented in this dissertation, future work that is of great interest includes, but not limit to, the following:

- Optimization of the PLD processes as well as the post-deposition annealing and ion etching processes for the realization of YIG nano films with even lower damping. The YIG nano films discussed in this dissertation were grown under the highest substrate temperature and lowest laser pulse repetition rate available in the author's laboratory. As discussed in Chapter 3, one can expect the realization of films with higher quality if an even higher substrate temperature and an even lower repetition rate are used. There should also exit an optimal etching time in the post-deposition ion etching process.

- Growth of YIG nano films by sputtering. Among various thin film deposition techniques, sputtering deposition usually has higher repeatability and is more extensively used in industry. Also, sputtered films usually have better uniformity and better stoichiometry than PLD films.

- Significant enhancement of spin transfer efficiency at YIG/NM interfaces through improvement of YIG-NM interface quality. One can improve the interface quality by carrying out appropriate treatments on YIG surfaces prior to the deposition of NM layers. Such surface treatments include cleaning with different chemicals, heating in particular environments, and low-energy ion etching.

- Suppression of Pt capping layer-caused damping. Chapter 6 demonstrates the feasibility of using a Cu spacer to suppress the new damping in YIG nano films due to Pt capping layers. In this aspect, two questions remain open: (1) Can one suppress the new damping by the use of a thin spacer made of other normal metals such as Au? (2) Will a YIG/Cu structure be more efficient than a YIG/Pt structure in terms of the production of spin currents by spin pumping? The future work will answer them.